

## ARTICLE

## OPEN



# Preparation of metrological states in dipolar-interacting spin systems

Tian-Xing Zheng <sup>1,2</sup>, Anran Li<sup>1,2</sup>, Jude Rosen <sup>1,2</sup>, Sisi Zhou<sup>1,3</sup>, Martin Koppenhöfer <sup>1</sup>, Ziqi Ma<sup>4,5</sup>, Frederic T. Chong<sup>4</sup>, Aashish A. Clerk <sup>1</sup>, Liang Jiang<sup>1</sup> and Peter C. Maurer<sup>1</sup>

Spin systems are an attractive candidate for quantum-enhanced metrology. Here we develop a variational method to generate metrological states in small dipolar-interacting spin ensembles with limited qubit control. For both regular and disordered spatial spin configurations the generated states enable sensing beyond the standard quantum limit (SQL) and, for small spin numbers, approach the Heisenberg limit (HL). Depending on the circuit depth and the level of readout noise, the resulting states resemble Greenberger-Horne-Zeilinger (GHZ) states or Spin Squeezed States (SSS). Sensing beyond the SQL holds in the presence of finite spin polarization and a non-Markovian noise environment. The developed black-box optimization techniques for small spin numbers ( $N \leq 10$ ) are directly applicable to diamond-based nanoscale field sensing, where the sensor size limits  $N$  and conventional squeezing approaches fail.

*npj Quantum Information* (2022)8:150 ; <https://doi.org/10.1038/s41534-022-00667-4>

## INTRODUCTION

Spin systems have emerged as a promising platform for quantum sensing<sup>1–4</sup> with applications ranging from tests of fundamental physics<sup>5,6</sup> to mapping fields and temperature profiles in condensed matter systems and life sciences<sup>3</sup>. Improving the sensitivity of these qubit sensors has so far largely relied on increasing the number of sensing spins and extending spin coherence through material engineering and coherent control. However, with increasing spin density, dipolar interactions between individual sensor spins cause single-qubit dephasing<sup>7,8</sup> and, in the absence of advanced dynamical decoupling<sup>9–11</sup>, set a limit to the sensitivity.

Although dipolar interactions in dense spin ensembles lead to complex evolution, they can provide a resource for the creation of metrological states that enable sensing beyond the SQL. Current approaches to create such states (i.e., GHZ states and SSS, see Supplementary Fig.1) either require all-to-all interactions<sup>12–15</sup> or single-qubit addressability<sup>16–18</sup>, which are challenging to implement experimentally. An alternative approach that relies on adiabatic state preparation requires less control but results in preparation times that increase exponentially with system size<sup>19,20</sup>, leaving this method susceptible to dephasing.

Variational methods provide a powerful tool for controlling many-body quantum systems<sup>21–23</sup>. Such methods have been proposed for Rydberg-interacting atomic systems<sup>24,25</sup> and demonstrated in trapped ions<sup>26</sup>. However, these techniques rely either on all-to-all interactions (i.e., trapped ions<sup>26</sup>) or strong coupling within a finite radius (i.e., Rydberg atoms<sup>24,27,28</sup>) which are generally absent in solid-state spin ensembles. In this work, we develop a variational algorithm that drives dipolar-interacting spin systems [Fig. 1(a)] into highly entangled states. The resulting states can be subsequently used for Ramsey-interferometry-based single parameter estimation<sup>1</sup>. The required system control relies solely on uniform single-qubit rotations and free evolution under dipolar interactions. Different spatial distributions of the spins (later referred as ‘spin configuration’) including 2D regular arrays and 3D random spin configurations

are investigated. The generated states resemble GHZ states or SSS depending on the spin-pattern geometry and the depth of the variational circuit. Experimental imperfections such as finite initialization/readout fidelity and dephasing noise are discussed for the example of a 2D regular array. The requirements on those imperfections for beating the SQL are given. Potential experimental platforms include dipolar-interacting ensembles of nitrogen-vacancy (NV) centers, nitrogen defects in diamond (P1), rare-earth-doped crystals, and ultra-cold molecules.

## RESULTS

### Variational ansatz

As shown in Fig. 1(b), the variational circuit  $\mathcal{S}(\boldsymbol{\theta}) = \mathcal{U}_m \dots \mathcal{U}_2 \mathcal{U}_1$  is constructed by  $m$  layers of unitary operations. Each  $\mathcal{U}_i$  consists of the parameterized control gates

$$\mathcal{U}_i = R_y\left(\frac{\pi}{2}\right)D(\tau'_i)R_y\left(-\frac{\pi}{2}\right)R_x(\vartheta_i)D(\tau_i), \quad (1)$$

where  $R_\mu(\vartheta) = \exp(-i\vartheta \sum_{j=1}^N S_j^\mu)$  are single-qubit rotations and  $S_j^\mu (\mu \in \{x, y, z\})$  is the  $\mu$  component of the  $j$ -th spin operator.  $D(\tau) = \exp(-i\tau H_{dd}/\hbar)$  is the time evolution operator of the spin ensemble under dipolar-interaction Hamiltonian  $H_{dd} = \sum_{i < j} V_{ij}(2S_i^z S_j^z - S_i^x S_j^x - S_i^y S_j^y)$ . The coupling strength between two spins at positions  $\mathbf{r}_i$  and  $\mathbf{r}_j$  is

$$V_{ij} = \frac{\mu_0}{4\pi} \frac{\gamma_i \gamma_j \hbar^2}{|\mathbf{r}_i - \mathbf{r}_j|^3} \frac{(1 - 3 \cos \beta_{ij})}{2}, \quad (2)$$

with  $\mu_0$  the vacuum permeability,  $\hbar$  the reduced Planck constant,  $\gamma$  the spin’s gyromagnetic ratio, and  $\beta_{ij}$  the angle between the line segment connecting  $(\mathbf{r}_i, \mathbf{r}_j)$  and the direction of bias magnetic field. An evolutionary algorithm<sup>29</sup> (Method) is applied on the  $m$ -layer circuit which contains  $3m$  free parameters constituting the vector  $\boldsymbol{\theta} = (\tau_1, \vartheta_1, \tau'_1, \dots, \tau_i, \vartheta_i, \tau'_i, \dots, \tau_m, \vartheta_m, \tau'_m)$ . Each  $\tau_i$  is restricted to  $\tau_i \in [0, 1/f_{dd}]$  where  $f_{dd}$  is the average nearest-neighbor interaction

<sup>1</sup>Pritzker School of Molecular Engineering, University of Chicago, Chicago, IL 60637, USA. <sup>2</sup>Department of Physics, University of Chicago, Chicago, IL 60637, USA. <sup>3</sup>Institute for Quantum Information and Matter, California Institute of Technology, Pasadena, CA 91125, USA. <sup>4</sup>Department of Computer Science, University of Chicago, Chicago, IL 60637, USA.

<sup>5</sup>Microsoft, Redmond, WA 98052, USA. email: pmaurer@uchicago.edu

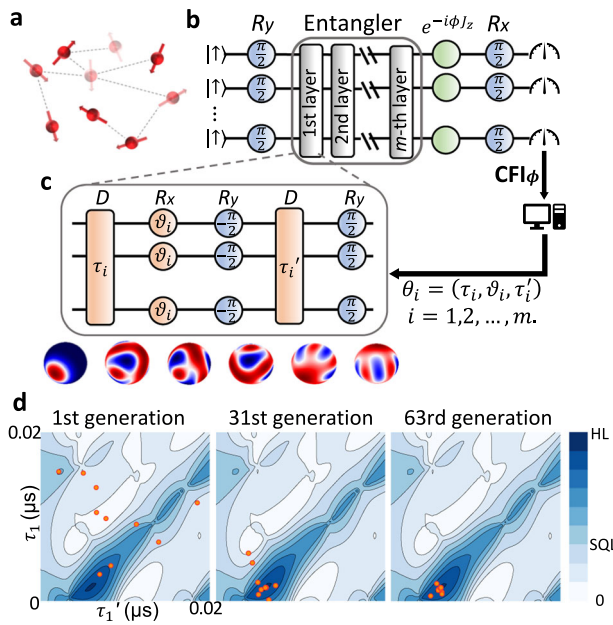


**Fig. 1 Preparation of metrological states by variational ansatz.** **a** Schematic of a dipolar-interacting spin ensemble in a 3D-random configuration. **b** The quantum circuit consists of three parts: a sequence for generating entanglement (entangler), phase accumulation (Ramsey) and single-qubit readout in the  $P_z$  basis. Dipolar interactions during Ramsey interference are eliminated by dynamical decoupling<sup>7,9,32</sup>. The measurement outcome is processed on a classical computer and used to determine the next generation for  $\theta$ . **c** Gate sequence of each variational layer and the Wigner distributions for a 5-spin state after each gate. **d** Illustration of an optimization process on a 3-spin system with  $m = 1$ . The contour plots show the 2D projection of the multidimensional  $\theta$  space for fixed  $\vartheta_1$ . The orange points mark the sampling positions in the parameter space. Convergence to the global maximum is reached in the 63rd generation.

strength for the considered spin configuration. After the metrological relevant states are generated by the variational ansatz, a Ramsey sequence<sup>1,30,31</sup> is applied to detect the external magnet field signal. During the Ramsey propagation<sup>1</sup> the spins accumulate a field dependent phase for a time  $\tau$ . Prior to the readout, a  $R_x(\pi/2)$  rotation converts this phase into a signal-dependent  $P_z$  expectation value. For the spin systems in which the dipolar interaction cannot be turned on and off at will, a Waugh-Huber-Haeberlen (WAUHUA) type dynamical decoupling sequence<sup>7,9,32</sup> is applied to cancel the dipolar interactions during the signal accumulation. The Ansatz in Eq. (1) is the most general set of global single-qubit gates that preserves the initial collective spin direction  $\langle \sum S_i \rangle / |\langle \sum S_i \rangle|$ , here chosen to be the  $x$ -direction<sup>24</sup>, Supplementary Note 1. Although this Ansatz does not enable universal system control<sup>33–35</sup>, Supplementary Discussion, we show that with increasing circuit depth, sensing near the HL can be achieved. A gradient-free black-box optimization algorithm is used for searching the parameter space  $\{\theta\}$  for an entangler that generates a desired metrological state. As shown in Fig. 1(d), the algorithm samples the parameter space  $\theta$  following a Gaussian distribution. In each generation, the algorithm iteratively updates the mean and variance of the Gaussian distribution according to the resulting cost function. This semi-random searching process is able to effectively jump out of local maxima.

### Metrological cost function

The Ramsey protocol shown in Fig. 1(b) encodes the quantity of interest in the accumulated phase  $\phi = \omega t_R$ , with  $\omega$  the detuning

frequency and  $t_R$  the Ramsey sensing time. The Classical Fisher Information (CFI)<sup>1</sup> quantifies how precisely one can estimate an unknown parameter  $\phi$  under a measurement basis. Our variational approach treats the spin systems as a black-box for which the algorithm finds a control sequence that maximizes the CFI associated with the parameter estimation problem

$$\text{CFI}_\phi = \sum_z \text{Tr}[P_z \rho_\phi] \left( \frac{\partial \log \text{Tr}[P_z \rho_\phi]}{\partial \phi} \right)^2. \quad (3)$$

The sum runs over the  $2^N$  basis states  $|z\rangle = \otimes_{i=1}^N |s_i^z\rangle$ , where  $s_i^z$  are the eigenvalues of  $S_i^z$ .  $P_z = |z\rangle \langle z|$  denotes the corresponding measurement operator and  $\rho_\phi$  the density matrix. The CFI is chosen as cost function because it quantifies the sensitivity of a measurement outcome to an external signal and measures the maximal achievable sensitivity for a given measurement basis<sup>1,36</sup>. Measurement operators such as parity ( $P_z^\text{tot}$ ) or total spin polarization ( $P_z^\text{tot}$ ) result in a smaller outcome space and are therefore more efficient in experimental implementations<sup>25,37–39</sup>, but contain less information than  $P_z$ . While we optimize the measurement for  $P_z$  in the main text, the obtained results also hold for measurements of  $P_z^\text{tot}$  and  $P_z^\text{tot}$ . We found that when measuring  $P_z^\text{tot}$  or  $P_z^\text{tot}$  the results improve when compared to  $P_z$ . Please check Supplementary Fig. 3 for detailed discussion.

### Numerical results for regular and disordered spin configurations

We start by testing our approach for three distinct regular spin configurations. Figure 2(a) shows the CFI after optimization for spins arranged on a linear chain (blue), a two-dimensional (2D) square lattice (orange), and a circle (green). All three configurations result in states with CFI above the SQL. When multiple circuit layers are added, the CFI further improves. Next, we simulate the case of disordered three-dimensional (3D) spin configurations (later referred as 3D-random). In our simulations the spins are randomly located in a box of length  $L \propto N^{1/3}$  (constant spin density). Compared to the regular spin array, the disordered case shows a noticeable saturation of the CFI as a function of  $N$  [Fig. 2(b)]. The  $N$  at which this saturation occurs can be increased by increasing the circuit depth [Fig. 2(c)]. This result for small  $N$  is different from the infinite sized systems where time evolution under dipolar interactions  $D(\tau)$  alone is not sufficient to generate metrologically useful entangled state (note, dipolar interactions in a 3D-random configuration average to zero, i.e.,  $\langle (1 - 3\cos^2\theta) \rangle = 0$ ). We attribute the observed metrological gain in Fig. 2(b) to a finite-size effects for small spin ensembles. This is in stark contrast to the 2D case where dipolar interaction does not average out<sup>40</sup> or regular 3D patterns<sup>41</sup>.

### Entanglement characterization

We investigate the  $N$ -qubit entangled states created by our variational method. The resulting states are visualized by plotting out the phase space quasiprobability distribution of the spin wavefunction in terms of the Wigner function (for more details on how the density matrix of a spin system is connected to the Wigner function, we refer to refs. 42–44; examples of Wigner distributions for specific states can be found in Supplementary Fig. 1). Figure 3(a) shows the corresponding Wigner distributions for a regular 2D spin array (top) and the average Wigner distributions for 50 different 3D-random spin configurations (bottom). In both cases, the optimized states resemble GHZ states when  $N$  is small and  $m$  is large. For large  $N$  and small  $m$ , the states are close to SSS. Non-Gaussian states that provide sensitivity beyond the SSS but lower than GHZ states are also generated. Our algorithm tends to drive the system into a GHZ state that lives in  $J = N/2$  total angular momentum subspace, as it has the unique property of attaining the HL in Ramsey spectroscopy<sup>45</sup>.

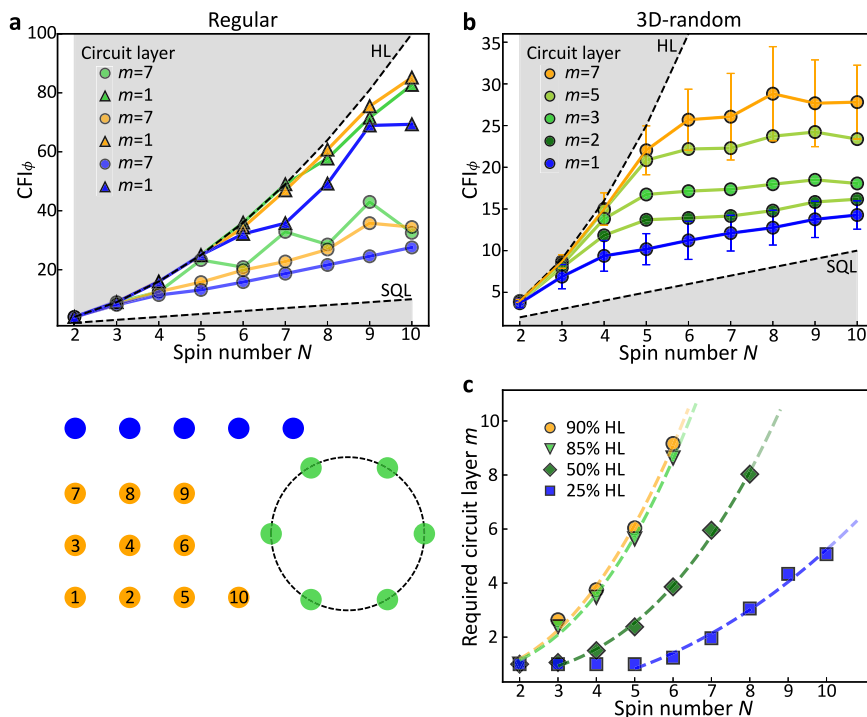
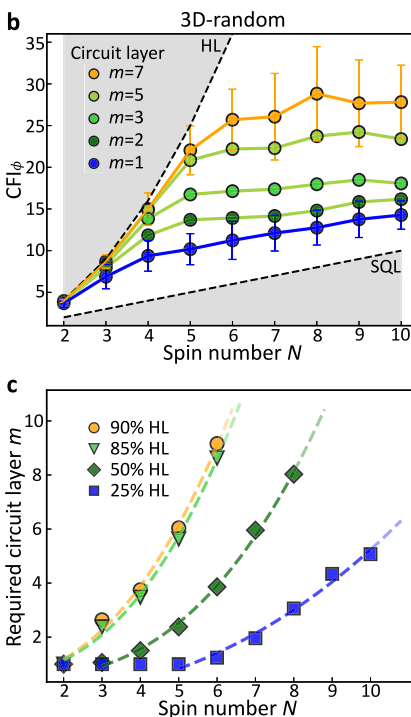


**Fig. 2 Optimization results of different spin configurations. a** Top: CFI for  $m = 1$  (circles) and  $m = 7$  (squares) circuits. The colors correspond to the configurations shown below. Bottom: schematics of different spin configurations. The numbers in the 2D square lattice pattern label the order in which spins are added to form a lattice of size  $N$ . **b** Average CFI for 50 configurations of 3D-randomly distributed spins. Error bars stand for the standard deviations of the optimized CFI from different spin configurations. (Error bars for  $m = 2, 3, 5$  are omitted for clear presentation). **c** Average number of layers required to achieve a CFI within a given percentage of the HL in the case of 3D-random configuration. The fit  $m = aN^b + c$  with  $b = 2.45$  (goodness of fit  $R^2 = 0.996$ ) serve as a guide to the eye. The same data also fits to an exponential model with slightly lower  $R^2 = 0.995$ . The investigation of deeper circuits becomes increasingly challenging as the efficiency of the employed optimization algorithm steeply decreases for  $m > 9$ . See Supplementary Figs. 2,5,6 and Supplementary Methods for more details.

For quantitatively analysing the build-up of entanglement, the von-Neumann entanglement entropy ( $E_{VN} = -\text{Tr}(\rho_s \log_2 \rho_s)$ )<sup>46</sup> was used as a measure for the degree of entanglement between a spin subsystem ( $\rho_s = \text{Tr}_{\bar{s}} \rho_{\text{tot}}$ ) and the remaining system. As an example, we explore one case of a 3D-random configuration of 9 spins. Figure 3(b) shows the von-Neumann entropy of each spin after employing a 2-layer circuit (left) and a 7-layer circuit (right). In the case of  $m = 2$ , the achieved degree of entanglement is modest with spin No.6 for example showing no substantial entanglement with the surrounding spins. When the circuit depth is increased to 7, all spins display substantial entanglement. While the single-particle entropy detects spins unentangled with the remaining system, it does not determine whether all spins are entangled with each other or entanglement is local. We distinguish these two scenarios by identifying the smallest clusters with  $E_{VN} \leq 0.4$ . For  $m = 2$ , the spin ensemble segments into 5 clusters [Fig. 3(b)], while for  $m = 7$  only 2 clusters are found. The results verify that multiple layers are required to overcome the anisotropy of the dipolar interaction [Eq. (2)] when building up entanglement over the entire system. Finally, in Fig. 3(c) we analyze the size of the largest cluster for each of the 50 spin configurations and observe an overall increase of the largest cluster size and a decrease of the variance.

#### State preparation time

Minimizing the preparation time is central in practical applications, as it increases bandwidth, reduces decoherence, and enables more measurement repetitions<sup>1</sup>. Figure 3(d) shows the average state preparation time for 8 spins in 50 different 3D-random configurations as a function of layer number. The preparation time



increases with the layer number and is inversely proportional to the average dipole coupling strength of the nearest-neighbor spins  $\bar{f}_{dd}$ . Compared to adiabatic methods<sup>19</sup>, our approach results in an  $11 \times$  reduction of the preparation time to reach the same CFI for identical spin number and density (see Supplementary Note 8 for detailed derivation). This is of particular importance when imperfections, such as dephasing, are taken into consideration.

#### State preparation under decoherence, initialization, readout and erasure errors

Until now our analysis assumed full coherence and perfect spin initialization and readout. We also assumed the spin configuration is fixed during each run of the optimization. However, dephasing, initialization, readout and erasure errors will be limiting factors in experimental implementations. We next examine the impact of such imperfections on state preparation and sensing. Figure 4(a) and (b) show the optimized CFI in the presence of imperfect initialization and finite readout fidelity for spins on a 2D square lattice. The algorithm is limited by computational resources and able to perform optimization for imperfect initialization for up to 8 spins. Beyond-SQL sensitivity is reached for 75% initialization fidelity (for  $N \leq 8$ ) and 92% readout fidelity (for  $N \leq 10$ ), respectively.

For further understanding the impact of readout fidelity on the optimized metrological states, we plot out the resulting states optimized under different readout fidelities. Figure 4(c) indicates that without readout errors, the Wigner distribution of the resulting state is close to a GHZ state. However, with a finite readout error rate, our algorithm drives the system into a state resembling a SSS. When the readout noise is further increased, the

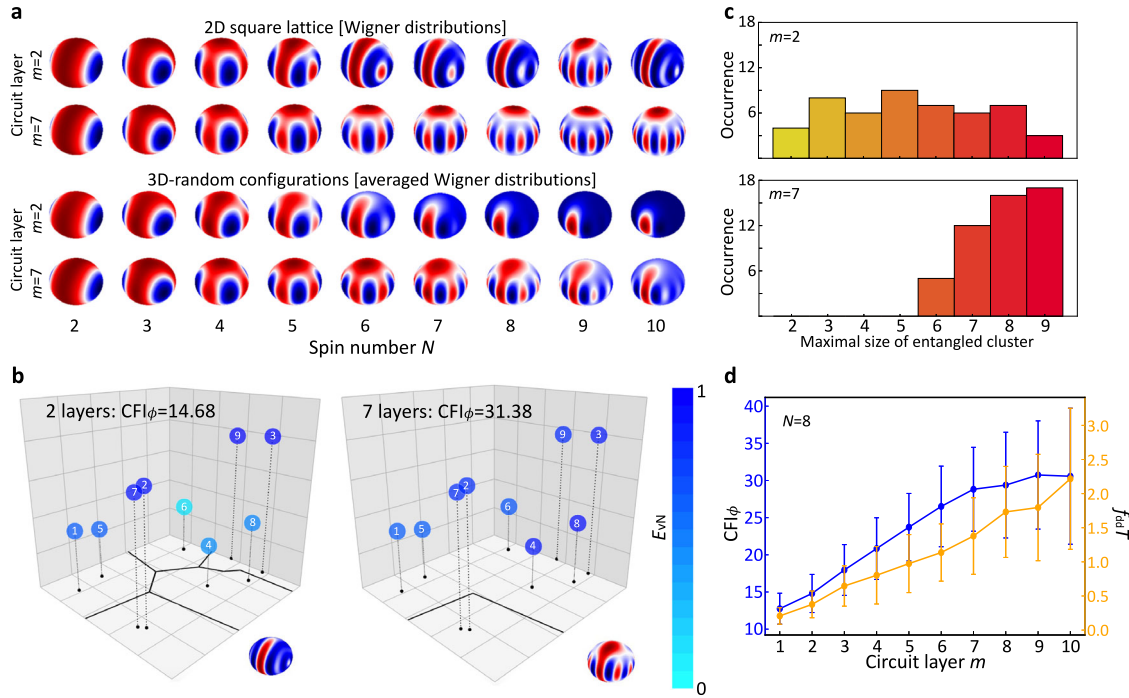


**Fig. 3 Entanglement build-up in metrological states.** **a** Wigner distributions versus spin number for  $m = 2$  and  $m = 7$  in the case of 2D square lattice and 3D-random configurations. The projected states into the  $J = N/2$  total angular momentum subspace are shown here. **b** von-Neumann entanglement entropy for one specific 3D-random configuration of 9 spins for  $m = 2$  and  $m = 7$ . Individual spins are labeled with an integer 1 through 9 to facilitate the discussion in the main text. The color of each data point corresponds to the von-Neumann entropy noted in the color bar to the right. Entangled clusters are marked by solid black lines. **c** Histograms depicting the maximal size of entangled clusters for 50 3D-random configurations. The number of spins per entangled clusters increases with circuit depth. **d** Average CFI (blue) and state preparation time (orange) versus  $m$ . Error bars indicate the standard deviations of CFI/state preparation time from different 3D random spin configurations. The state preparation time is given as a unitless quantity  $\bar{f}_{dd} T$  with  $T = \sum_{i=1}^m (\tau_i + \tau'_i)$ .

SSS transforms into a coherent spin state (CSS). The results agree with the fact that GHZ states are sensitive to single-spin readout errors while SSS are more robust<sup>47</sup>.

In addition to the discussed spin readout and initialization errors many experimental platforms also suffer from changing spin configurations between consecutive runs. This so-called erasure error is caused by a finite ionization/deionization rate in the case of NV centers<sup>48,49</sup> and a finite loading possibility in the case of cold molecules<sup>50</sup>. Figure 4(d) shows the optimized average CFI versus the average number of loaded spins  $N^*$  per cycle. The obtained results indicate that our approach is comparable robust to erasure errors, with beyond-SQL sensitivity for loading efficiencies as low as 50%.

During the state preparation, decoherence ( $T_2$ ) reduces entanglement. We assume independent, Markovian dephasing of each spin as described by a Lindblad master equation<sup>46</sup>. Figure 4(e) shows the CFI for various  $T_2$  times using the previously optimized gate parameters for 2D square lattice. While a finite  $T_2$  decreases the CFI, coherence times exceeding  $0.5/f_{dd}$  result in states with beyond-SQL sensitivity for  $N \leq 8$ . Here,  $f_{dd}$  denotes the nearest-neighbor interaction strength for 2D square lattice. For small  $T_2$  the resulting state will converge toward a CSS, which results in a sensitivity set by the SQL.

### Sensitivity in a non-Markovian environment

In addition to impacts on state preparation, dephasing affects performance in Ramsey interferometry. In the presence of spatially uncorrelated Markovian noise, entanglement does not lead to a beyond-SQL scaling<sup>51,52</sup>. In a non-Markovian environment, this limitation does not hold<sup>53–55</sup>. Such as in a solid-state spin system, slow evolution of nuclear spins leads to correlated noise<sup>8,56</sup> on the sensing qubit. We examine the performance of our optimized states

in a non-Markovian noise environment. We adopt a noise model<sup>53</sup> in which the amplitude of single-spin coherence reduces according to

$$\rho_{01}(t) = \rho_{01}(0) e^{-\left(\frac{t}{T_2}\right)^v} \quad (4)$$

where  $v$  is the stretch factor set by the noise properties. The time evolution under Ramsey propagation is simulated with a generalized Lindblad master equation<sup>54</sup>. The sensing performance of optimized states is characterized by the square of the signal-noise-ratio  $\text{SNR}^2 \propto \text{CFI}_\omega / T_R$  (see Supplementary Notes 2–7). Figure 4(f) shows their performance compared to the CSS and the GHZ states for a  $v=2$  and  $v=4$  noise exponent<sup>8</sup>. The created entangled states provide an advantage over uncorrelated states. For small spin numbers, the SNR follows the HL scaling<sup>53</sup>.

### Proposed experimental platforms

Candidate systems for realizing the proposed variational approach need to possess long  $T_2$  coherence time, strong dipolar-interacting strength, and high initialization and readout fidelity. Recent developments in solid-state spin systems and ultracold molecules have demonstrated coherence times that exceed dipolar coupling times ( $1/f_{dd}$ ) as well as high-fidelity spin initialization and readout. Table 1 lists the experimentally observed parameters for different candidate systems, including NV ensembles, P1 centers in diamond, rare-earth doped crystals, and ultracold molecule tweezer systems.

The listed  $T_2^{(DD)}$  in Table 1 are lower bounds for the actual  $T_2$ . Specifically,  $T_2^{(DD)}$  represent the experimental coherence measured under WAHUA-type dynamical decoupling, which contains remaining dephasing terms caused by dipolar interaction<sup>11</sup>. On the other hand, our protocol relies on the presence of dipolar interaction for the generation of the desired entangled states. Therefore dipolar

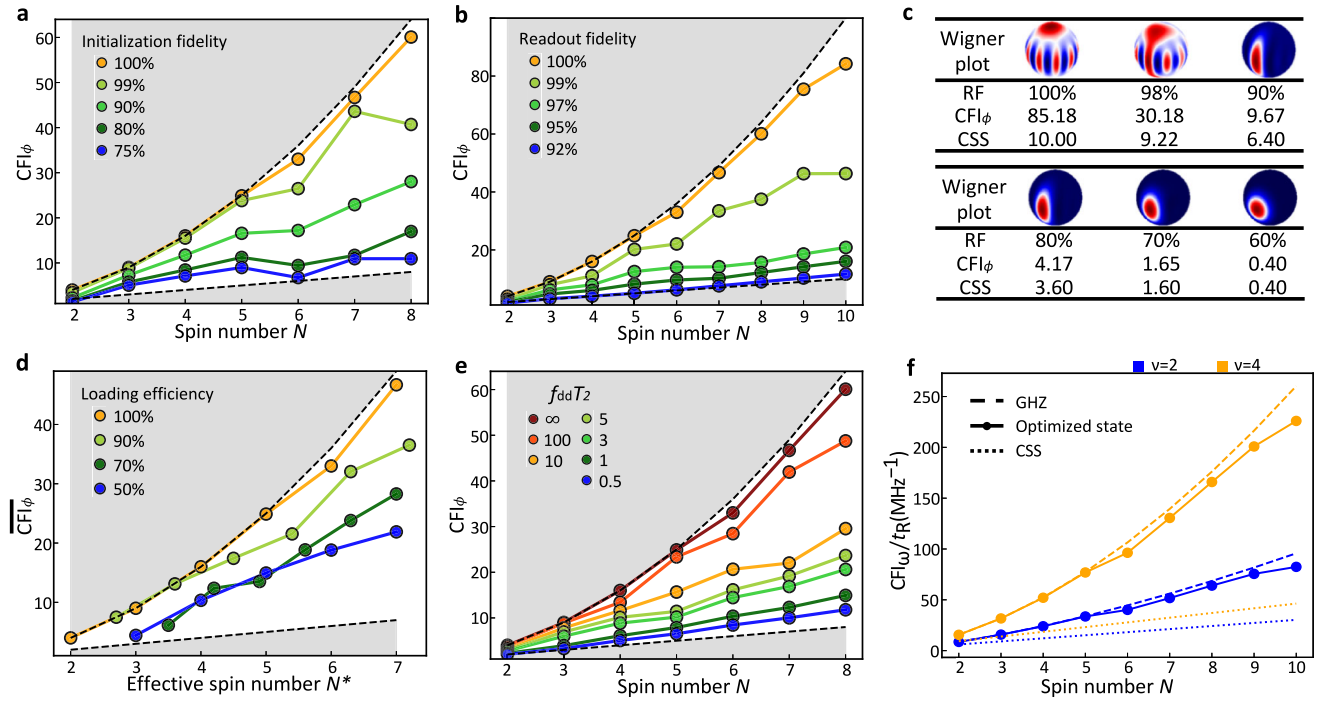


**Fig. 4 Performance under imperfections.** **a**  $\text{CFI}_\phi$  under finite initialization fidelity (IF). IF.  $\text{IF} = \frac{N_\uparrow - N_\downarrow}{N}$ , where  $N_\uparrow$  ( $N_\downarrow$ ) denotes the number of spins in the  $|\uparrow\rangle$  ( $|\downarrow\rangle$ ) state at the beginning of the sensing protocol in Fig. 1(b). **b**  $\text{CFI}_\phi$  under finite readout fidelity (RF). RF.  $\text{RF} = 1 - p(|\downarrow\rangle|\uparrow\rangle) = 1 - p(|\uparrow\rangle|\downarrow\rangle)$ . **c** Optimized Wigner functions and  $\text{CFI}_\phi$  of a 10-spin state versus different readout fidelities (RF). For comparison, the row ‘CSS’ represents the  $\text{CFI}_\phi$  for a coherent spin state given the same RF. See Supplementary Fig. 9 for more information. **d** Average  $\text{CFI}_\phi$  under finite loading efficiency. Effective spin number  $N^*$  is the averagely loaded spin number for a given configuration and loading efficiency. **e**  $\text{CFI}_\phi$  in the presence of decoherence in the entangler. **f** Ramsey protocol’s results of the generated states when considering non-Markovian noise during signal accumulation (see Supplementary Fig. 8 for more details). All data correspond to the optimized states from 2D square lattice configuration using a 5-layer circuit.

**Table 1.** Parameters of different experimental platforms.

Systems	$\bar{f}_{dd}$	$T_2^{(DD)}$	$\bar{f}_{dd}T_2^{(DD)}$	$P_{ini}$	$F_{readout}$	$v$
NV ensemble	35 kHz <sup>32</sup>	7.9(2) $\mu\text{s}^{32}$	0.28	97.5% <sup>69</sup>	97.5% <sup>69</sup>	2 – 4 <sup>8</sup>
P1 centers	0.92 MHz <sup>70</sup>	4.4 $\mu\text{s}^{70}$	4.0	95% <sup>71</sup>	95% <sup>71</sup>	?
Rare-Earth crystals	1.96 MHz <sup>72</sup>	2.5 $\mu\text{s}^{72}$	4.9	97% <sup>17</sup>	94.6% <sup>73</sup>	$2.4 \pm 0.1^{56}$
Cold Molecules	52 Hz <sup>7</sup>	80 ms <sup>7</sup>	4.16	97% <sup>50</sup>	97% <sup>50</sup>	?

interaction between spins is part of the system Hamiltonian that does not contribute to dephasing during the state preparation. Thus, the relevant coherence is the single particle  $T_2$  in the absence of dipolar spin-spin interacting (see Supplementary Table 1).

## DISCUSSION

This work introduces a variational circuit that efficiently generates entangled metrological states in a dipolar-interacting spin system. The required system parameters are within the reach of several experimental platforms. When directly running this variational method on an experimental platform, metrological states can be generated without the prior knowledge of the actual spin locations. While this study remains limited to small system sizes ( $N \leq 10$ , limited by computational resource), our results are of immediate interest to nanoscale quantum sensing where spatial resolution is

paramount and the finite sensor size limits the number of spins that can be utilized. Specific examples include the investigation of 2D materials<sup>57–60</sup>, structures and dynamics of magnetic domains<sup>61,62</sup>, vortex structures in superconductivity<sup>63,64</sup>, and magnetic resonance spectroscopy on individual proteins and DNA molecules<sup>65–68</sup>.

Extending our investigation to  $N > 10$  can either be achieved by utilizing symmetries in regular arrays or directly testing our optimization algorithms on an actual experimental platform. The developed method is also potentially applicable to preparing other highly entangled states relevant to quantum computing and quantum communication.

## METHOD

### Gradient-free optimization: CMA-ES

The optimization in the  $3m$  dimensional parameter space is highly non-convex [Fig. 1(d)] due to the large inhomogeneity of the interaction strength. In our setting, the previously used Dividing Rectangles algorithm<sup>22,24</sup> cannot converge to a beyond-SQL result despite large number of iterations. We address this challenge by using the Covariance Matrix Adaptation Evolution Strategy (CMA-ES) as our optimization algorithm<sup>29</sup>. CMA-ES balances the exploration and exploitation process when searching in the parameter space so that convergence is reached after  $\sim 2000$  generations for  $N, m \leq 10$ . This corresponds to about  $10^8$  repetitions of the Ramsey experiment, which can be further reduced if collective measurement observables are measured (Supplementary Fig. 3).

We reduce the complexity of the optimization by restricting  $\tau_i$  within  $[0, 1/\bar{f}_{dd}]$  where  $\bar{f}_{dd}$  is the average nearest-neighbor interaction strength for the considered spin configuration. Setting a large parameter searching range for the interaction gates’ time  $\tau_i$

would potentially ensure the global maximum CFI location is included in the parameter space. However, when the upper bound of  $\tau_i$  is much bigger than  $1/\bar{f}_{dd}$ , the evolution of neighboring spin pairs is fast when sweeping  $\tau_i$ . This would introduce a huge amount of local maximum points in the parameter search so that it is impractical for the black-box optimization algorithm to converge to that global maximum point. A good value for  $\bar{f}_{dd}$  can be estimated from the doping level of the spin defects (NV, P1, rare-earth ions) or the distance between the cold molecule tweezers. Measuring the fast oscillation frequency in Ramsey experiments will also provide an estimate of the  $\bar{f}_{dd}$ .

## DATA AVAILABILITY

All relevant data supporting the main conclusions and figures of the document are available from the corresponding author on reasonable request.

## CODE AVAILABILITY

All relevant code is available from the corresponding author upon reasonable request.

Received: 16 June 2022; Accepted: 7 December 2022;

Published online: 22 December 2022

## REFERENCES

- Degen, C. L., Reinhard, F. & Cappellaro, P. Quantum sensing. *Rev. Mod. Phys.* **89**, 035002 (2017).
- Barry, J. F. et al. Sensitivity optimization for NV-diamond magnetometry. *Rev. Mod. Phys.* **92**, 015004 (2020).
- Schiragh, R., Chang, K., Loretz, M. & Degen, C. L. Nitrogen-vacancy centers in diamond: nanoscale sensors for physics and biology. *Annu. Rev. Phys. Chem.* **65**, 83–105 (2014).
- Tetienne, J.-P. Quantum sensors go flat. *Nat. Phys.* **17**, 1074–1075 (2021).
- Hensen, B. et al. Loophole-free Bell inequality violation using electron spins separated by 1.3 kilometres. *Nature* **526**, 682–686 (2015).
- Marti, G. E. et al. Imaging optical frequencies with 100  $\mu$ Hz precision and 1.1  $\mu$ m resolution. *Phys. Rev. Lett.* **120**, 103201 (2018).
- Yan, B. et al. Observation of dipolar spin-exchange interactions with lattice-confined polar molecules. *Nature* **501**, 521–525 (2013).
- Childress, L. et al. Coherent dynamics of coupled electron and nuclear spin qubits in diamond. *Science* **314**, 281–285 (2006).
- Waugh, J. S., Huber, L. M. & Haeberlen, U. Approach to high-resolution NMR in solids. *Phys. Rev. Lett.* **20**, 180 (1968).
- Mehring, M. *Principles of high resolution NMR in solids* (Springer Science & Business Media, 2012).
- Choi, J. et al. Robust dynamic hamiltonian engineering of many-body spin systems. *Phys. Rev. X* **10**, 031002 (2020).
- Pedrozo-Pé nafield, E. et al. Entanglement on an optical atomic-clock transition. *Nature* **588**, 414–418 (2020).
- Kitagawa, M. & Ueda, M. Squeezed spin states. *Phys. Rev. A* **47**, 5138 (1993).
- Li, Z. et al. Collective spin-light and light-mediated spin-spin interactions in an optical cavity. *PRX Quant.* **3**, 020308 (2022).
- Bilitewski, T. et al. Dynamical generation of spin squeezing in ultracold dipolar molecules. *Phys. Rev. Lett.* **126**, 113401 (2021).
- Koczor, B., Endo, S., Jones, T., Matsuzaki, Y. & Benjamin, S. C. Variational-state quantum metrology. *N. J. Phys.* **22**, 083038 (2020).
- Chen, S., Raha, M., Phenican, C. M., Ourari, S. & Thompson, J. D. Parallel single-shot measurement and coherent control of solid-state spins below the diffraction limit. *Science* **370**, 592–595 (2020).
- Neumann, P. et al. Multipartite entanglement among single spins in diamond. *Science* **320**, 1326–1329 (2008).
- Cappellaro, P. & Lukin, M. D. Quantum correlation in disordered spin systems: Applications to magnetic sensing. *Phys. Rev. A* **80**, 032311 (2009).
- Choi, S., Yao, N. Y. and Lukin, M. D. Quantum metrology based on strongly correlated matter Preprint at <https://arxiv.org/abs/1801.00042> (2017).
- Cerezo, M. et al. Variational quantum algorithms. *Nat. Rev. Phys.* **3**, 625–644 (2021).
- Kokail, C. et al. Self-verifying variational quantum simulation of lattice models. *Nature* **569**, 355–360 (2019).
- Ebadi, S. et al. Quantum optimization of maximum independent set using Rydberg atom arrays. *Science* **376**, 1209–1215 (2022).
- Kaibrugeger, R. et al. Variational spin-squeezing algorithms on programmable quantum sensors. *Phys. Rev. Lett.* **123**, 260505 (2019).
- Kaibrugeger, R., Vasilyev, D. V., Schulte, M., Hammerer, K. & Zoller, P. Quantum variational optimization of Ramsey interferometry and atomic clocks. *Phys. Rev. X* **11**, 2160 (2021).
- Marciniak, C. D. et al. Optimal metrology with programmable quantum sensors. *Nature* **603**, 604–609 (2022).
- Borish, V., Marković, O., Hines, J. A., Rajagopal, S. V. & Schleier-Smith, M. Transverse-field Ising dynamics in a Rydberg-dressed atomic gas. *Phys. Rev. Lett.* **124**, 063601 (2020).
- Bernien, H. et al. Probing many-body dynamics on a 51-atom quantum simulator. *Nature* **551**, 579–584 (2017).
- Hansen, N. The CMA evolution strategy: a tutorial Preprint at <https://arxiv.org/abs/1604.00772> (2016).
- Ramsey, N. F. A molecular beam resonance method with separated oscillating fields. *Phys. Rev.* **78**, 695 (1950).
- Taylor, J. M. et al. High-sensitivity diamond magnetometer with nanoscale resolution. *Nat. Phys.* **4**, 810–816 (2008).
- Zhou, H. et al. Quantum metrology with strongly interacting spin systems. *Phys. Rev. X* **10**, 031003 (2020).
- Schirmer, S. G., Fu, H. & Solomon, A. I. Complete controllability of quantum systems. *Phys. Rev. A* **63**, 063410 (2001).
- Albertini, F. & D'Alessandro, D. The lie algebra structure and controllability of spin systems. *Linear Algebra Appl.* **350**, 213–235 (2002).
- Albertini, F. & D'Alessandro, D. Subspace controllability of multi-partite spin networks. *Syst. Control. Lett.* **151**, 104913 (2021).
- Kobayashi, H., Mark, B. L. & Turin, W. *Probability, random processes, and statistical analysis* (Cambridge University Press, 2011).
- Davis, E., Bentsen, G. & Schleier-Smith, M. Approaching the heisenberg limit without single-particle detection. *Phys. Rev. Lett.* **116**, 053601 (2016).
- Strobel, H. et al. Fisher information and entanglement of non-gaussian spin states. *Science* **345**, 424–427 (2014).
- Colombo, S. et al. Time-reversal-based quantum metrology with many-body entangled states. *Nat. Phys.* **18**, 925–930 (2022).
- Davis, E. J. et al. Probing many-body noise in a strongly interacting two-dimensional dipolar spin system Preprint at <https://arxiv.org/abs/2103.12742> (2021).
- Perlin, M. A., Qu, C. & Rey, A. M. Spin squeezing with short-range spin-exchange interactions. *Phys. Rev. Lett.* **125**, 223401 (2020).
- Hillery, M., O'Connell, R. F., Scully, M. O. & Wigner, E. P. Distribution functions in physics: Fundamentals. *Phys. Rep.* **106**, 121–167 (1984).
- Dowling, J. P., Agarwal, G. S. & Schleich, W. P. Wigner distribution of a general angular-momentum state: applications to a collection of two-level atoms. *Phys. Rev. A* **49**, 4101 (1994).
- Koczor, B., Zeier, R. & Glaser, S. J. Fast computation of spherical phase-space functions of quantum many-body states. *Phys. Rev. A* **102**, 062421 (2020).
- Giovannetti, V., Lloyd, S. & Maccone, L. Quantum metrology. *Phys. Rev. Lett.* **96**, 010401 (2006).
- Nielsen, M. A. and Chuang, I. L. *Quantum Computation and Quantum Information: 10th Anniversary Edition* (Cambridge University Press, 2010). <https://doi.org/10.1017/CBO9780511976667>.
- Davis, E., Bentsen, G., Li, T. & Schleier-Smith, M. Advantages of interaction-based readout for quantum sensing. *Adv. Photon. Quant. Comput. Mem. Commun. X* **10118**, 101180Z (2017).
- Doherty, M. W. et al. The nitrogen-vacancy colour centre in diamond. *Phys. Rep.* **528**, 1–45 (2013).
- Razinkovas, L., Maciaszek, M., Reinhard, F., Doherty, M. W. & Alkauskas, A. Photoionization of negatively charged NV centers in diamond: Theory and ab initio calculations. *Phys. Rev. B* **104**, 235301 (2021).
- Cheuk, L. W. et al. Observation of collisions between two ultracold ground-state caf molecules. *Phys. Rev. Lett.* **125**, 043401 (2020).
- Demkowicz-Dobrzański, R., Kołodyński, J. & Guță, M. The elusive heisenberg limit in quantum-enhanced metrology. *Nat. Commun.* **3**, 1063 (2012).
- Escher, B., de Matos Filho, R. & Davidovich, L. General framework for estimating the ultimate precision limit in noisy quantum-enhanced metrology. *Nat. Phys.* **7**, 406–411 (2011).
- Chin, A. W., Huelga, S. F. & Plenio, M. B. Quantum metrology in non-markovian environments. *Phys. Rev. Lett.* **109**, 233601 (2012).
- Smirne, A., Kołodyński, J., Huelga, S. F. & Demkowicz-Dobrzański, R. Ultimate precision limits for noisy frequency estimation. *Phys. Rev. Lett.* **116**, 120801 (2016).
- Matsuzaki, Y., Benjamin, S. C. & Fitzsimons, J. Magnetic field sensing beyond the standard quantum limit under the effect of decoherence. *Phys. Rev. A* **84**, 012103 (2011).

56. Le Dantec, M. et al. Twenty-three-millisecond electron spin coherence of erbium ions in a natural-abundance crystal. *Sci. Adv.* **7**, 51 (2021).
57. Casola, F., Van Der Sar, T. & Yacoby, A. Probing condensed matter physics with magnetometry based on nitrogen-vacancy centres in diamond. *Nat. Rev. Mater.* **3**, 1–13 (2018).
58. Vool, U. et al. Imaging phonon-mediated hydrodynamic flow in WTe<sub>2</sub>. *Nat. Phys.* **17**, 1216–1220 (2021).
59. Jenkins, A. et al. Imaging the breakdown of ohmic transport in graphene. *Phys. Rev. Lett.* **129**, 087701 (2022).
60. Palm, M. L. et al. Imaging of submicroampere currents in bilayer graphene using a scanning diamond magnetometer. *Phys. Rev. Appl.* **17**, 054008 (2022).
61. Tetienne, J. P. et al. The nature of domain walls in ultrathin ferromagnets revealed by scanning nanomagnetometry. *Nat. Commun.* **6**, 6733 (2015).
62. Gross, I. et al. Real-space imaging of non-collinear antiferromagnetic order with a single-spin magnetometer. *Nature* **549**, 252–256 (2017).
63. Pelliccione, M. et al. Scanned probe imaging of nanoscale magnetism at cryogenic temperatures with a single-spin quantum sensor. *Nat. Nanotechnol.* **11**, 700–705 (2016).
64. Scheidegger, P. J., Diesch, S., Palm, M. L. & Degen, C. Scanning nitrogen-vacancy magnetometry down to 350 mK. *Appl. Phys. Lett.* **120**, 224001 (2022).
65. Staudacher, T. et al. Nuclear magnetic resonance spectroscopy on a (5-nanometer) 3 sample volume. *Science* **339**, 561–563 (2013).
66. Shi, F. et al. Single-protein spin resonance spectroscopy under ambient conditions. *Science* **347**, 1135–1138 (2015).
67. Shi, F. et al. Single-DNA electron spin resonance spectroscopy in aqueous solutions. *Nat. Methods* **15**, 697–699 (2018).
68. Lovchinsky, I. et al. Nuclear magnetic resonance detection and spectroscopy of single proteins using quantum logic. *Science* **351**, 836–841 (2016).
69. Shields, B. J., Unterreithmeier, Q. P., de Leon, N. P., Park, H. & Lukin, M. D. Efficient readout of a single spin state in diamond via spin-to-charge conversion. *Phys. Rev. Lett.* **114**, 136402 (2015).
70. Zu, C. et al. Emergent hydrodynamics in a strongly interacting dipolar spin ensemble. *Nature* **597**, 45–50 (2021).
71. Degen, M. et al. Entanglement of dark electron-nuclear spin defects in diamond. *Nat. Commun.* **12**, 3470 (2021).
72. Merkel, B., Farina, P. C. & Reiserer, A. Dynamical decoupling of spin ensembles with strong anisotropic interactions. *Phys. Rev. Lett.* **127**, 030501 (2021).
73. Raha, M. et al. Optical quantum nondemolition measurement of a single rare earth ion qubit. *Nat. Commun.* **11**, 1605 (2020).

## ACKNOWLEDGEMENTS

We thank D. DeMille, D. Freedmann, A. Bleszynski Jayich, S. Kolkowitz, T. Li, Z. Li, R. Kaubriegger, Y. Huang, Q. Xuan, Z. Zhang, S. von Kugelgen, C.-J. Yu, Y. Bao, P. Gokhale, N. Leitao, L. Martin and H. Zhou for helpful discussions. The investigation of sensing performance and state preparation under noise is based upon work supported by Q-NEXT (Grant No. DOE 1F-60579), one of the U.S. Department of Energy Office of Science National Quantum Information Science Research Centers. T.-X.Z. and P.C.M. acknowledge support by National Science Foundation (NSF) Grant No. OMA-1936118 and OIA-2040520, and NSF QuBBE QLCI (NSF OMA-2121044). S.Z. acknowledges funding provided by the Institute for Quantum Information and

Matter, an NSF Physics Frontiers Center (NSF Grant PHY-1733907). Z.M. and F.T.C. acknowledge support by EPiQC, an NSF Expedition in Computing, under grants CCF-1730082/1730449; in part by STAQ under grant NSF Phy-1818914; in part by the US DOE Office of Advanced Scientific Computing Research, Accelerated Research for Quantum Computing Program.; and in part by NSF OMA-2016136. The authors are also grateful for the support of the University of Chicago Research Computing Center for assistance with the numerical simulations carried out in this work.

## AUTHOR CONTRIBUTIONS

T.-X.Z., A.L., and J.R. designed and wrote the numerical simulations. T.-X.Z., A.L., J.R., S.Z., M.K., and Z.M. analyzed the results. F.T.C., A.A.C., L.J. and P.C.M. provided guidance. P.C.M. developed the idea and supervised the project. All authors contributed to discussing the results and writing the paper.

## COMPETING INTERESTS

F.T.C. is the Chief Scientist for Quantum Software at ColdQuanta and an advisor to Quantum Circuits, Inc. The authors declare that there are no other competing interests.

## ADDITIONAL INFORMATION

**Supplementary information** The online version contains supplementary material available at <https://doi.org/10.1038/s41534-022-00667-4>.

**Correspondence** and requests for materials should be addressed to Peter C. Maurer.

**Reprints and permission information** is available at <http://www.nature.com/reprints>

**Publisher's note** Springer Nature remains neutral with regard to jurisdictional claims in published maps and institutional affiliations.



**Open Access** This article is licensed under a Creative Commons Attribution 4.0 International License, which permits use, sharing, adaptation, distribution and reproduction in any medium or format, as long as you give appropriate credit to the original author(s) and the source, provide a link to the Creative Commons license, and indicate if changes were made. The images or other third party material in this article are included in the article's Creative Commons license, unless indicated otherwise in a credit line to the material. If material is not included in the article's Creative Commons license and your intended use is not permitted by statutory regulation or exceeds the permitted use, you will need to obtain permission directly from the copyright holder. To view a copy of this license, visit <http://creativecommons.org/licenses/by/4.0/>.

© The Author(s) 2022

# Supplemental Information for: Preparation of Metrological States in Dipolar Interacting Spin Systems

Tian-Xing Zheng<sup>1,2</sup>, Anran Li<sup>1</sup>, Jude Rosen<sup>1</sup>, Sisi Zhou<sup>1,3</sup>, Martin Koppenhöfer<sup>1</sup>, Ziqi Ma<sup>4,5</sup>, Frederic T. Chong<sup>4</sup>, Aashish A. Clerk<sup>1</sup>, Liang Jiang<sup>1</sup>, and Peter C. Maurer<sup>1</sup><sup>✉</sup>

<sup>1</sup>*Pritzker School of Molecular Engineering, University of Chicago, Chicago, Illinois 60637, USA*

<sup>2</sup>*Department of Physics, University of Chicago, Chicago, Illinois 60637, USA*

<sup>3</sup>*Institute for Quantum Information and Matter,*

*California Institute of Technology, Pasadena, California 91125, USA*

<sup>4</sup>*Department of Computer Science, University of Chicago, Chicago, Illinois 60637, USA*

<sup>5</sup>*Microsoft, Redmond, Washington 98052, USA and*

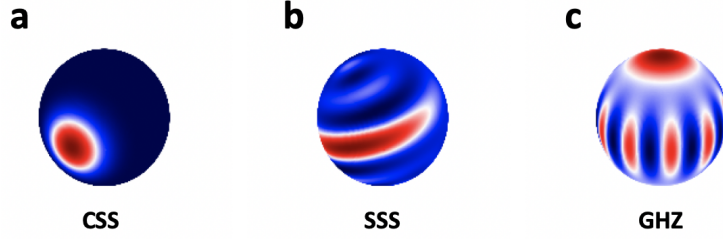
<sup>✉</sup>*email: pmaurer@uchicago.edu*

## CONTENTS

Supplementary Figures	2
Supplementary Figure 1: Wigner function and standard metrological states	2
Supplementary Figure 2: Optimization results of different types of dipole-dipole interaction Hamiltonian	2
a. NV ensemble	3
b. Ising type interaction (large local disorder)	3
Supplementary Figure 3: Optimization results by using $P_z^{\text{tot}}$ , $P_z^{\pi}$ as measurement bases	4
Supplementary Figure 4: Mutual Information of the Metrological States	5
Supplementary Figure 5: Complete CFI data for Fig.2 in main text	6
Supplementary Figure 6: Required layers to reach given CFI for 2D square lattice	7
Supplementary Figure 7: Orders of interaction	7
Supplementary Figure 8: Non-Markovian noise sensing performance in 3D random spin configurations	8
Supplementary Figure 9: Optimized states with different readout fidelity	8
Supplementary Tables	9
Supplementary Table 1: Relative experimental parameter table (full)	9
Supplementary Notes	10
Supplementary Note 1: Designing the variational circuit	10
c. Entanglement generation gates from two-body interaction Hamiltonian and global rotations	10
d. Preservation of the collective spin direction	10
e. Choosing the most general gate set	11
Supplementary Note 2: CFI with respect to angle and frequency	11
Supplementary Note 3: Relation between CFI $_{\omega}$ and SNR in single qubit Ramsey experiment	13
Supplementary Note 4: Maximum Likelihood Estimator	14
Supplementary Note 5: Master equation for a non-Markovian environment	16
Supplementary Note 6: Performance of metrological states in a non-Markovian environment	19
Supplementary Note 7: Time Overhead	19
Supplementary Note 8: State preparation time comparing to adiabatic method	20
Supplementary Note 9: Numerically solving Schrödinger and Lindblad equations	21
Supplementary Discussion: Controllability	21
Controllability Test	22
Controllability of Dipolar Interacting Spin Systems	22
Finding Reachable States	23
Supplementary Methods	23
Large spin number ( $N \rightarrow 100$ ) optimization: discrete truncated Wigner approximation (DTWA)	23
Supplementary References	25

## SUPPLEMENTARY FIGURES

**Supplementary Figure 1:** Wigner function and standard metrological states



**Supplementary Figure 1. Three standard metrological states:** Spin number  $N = 10$ . (a) Coherent Spin State (CSS). (b) Spin Squeezed States (SSS). Generated by one-axis twisting  $H_{OAT} = \chi J_z^2$ ,  $\chi t = 0.3$ . (C) Greenberger-Horne-Zeilinger (GHZ) state.

The Wigner function of the spin system provides an intuitive visualization tool of the spin wavefunction. It maps the permutation symmetric subspace ( $J = N/2$ ) of the  $N$  spin-1/2 system onto a quasiprobability distribution in the phase space by calculating the expectation value of the rotated parity operator:

$$W_\rho(\theta, \phi) = \text{Tr}[\rho R(\theta, \phi) M_0 R^\dagger(\theta, \phi)]. \quad (1)$$

The parity operator,

$$M_0 = \frac{2\pi}{J} \sum_{j=0}^{j=2J} \sqrt{\frac{2j+1}{4\pi}} T_{j0}, \quad (2)$$

Is the weighted sum of zeroth-order tensor operators  $[T_{j0}]_{mm'} = \delta_{mm'} \sqrt{(2j+1)/(2J+1)} C_{Jm,j0}^{Jm}$ . Here,  $C_{Jm,j0}^{Jm}$  is a Clebsch-Gordan coefficient [1].

In Fig. 1, three standard metrological states are plotted. Coherent Spin State (CSS) is the classical state which reaches SQL and it's the suitable state for sensing when there is Markovian noise during the Ramsey time or when the experimental readout noise is high. Spin Squeezed States (SSS) beat the SQL by their squeezed variance of the spin angular momentum along the signal direction. Greenberger-Horne-Zeilinger (GHZ) states are able to reach the HL by utilizing the  $N$  fringes perpendicular to the equator to detect the external field simultaneously. All these standard metrological states lie in the permutation symmetric  $J = N/2$  subspace, so the Wigner function plots in the main text are able to capture the essential features of the optimized metrological states.

**Supplementary Figure 2: Optimization results of different types of dipole-dipole interaction Hamiltonian**

The magnetic dipole-dipole interaction Hamiltonian under secular approximation has the general form [2, 3]:

$$H_{dd} = \sum_{i < j} V_{ij} (2S_{zi}S_{zj} - S_{xi}S_{xj} - S_{yi}S_{yj}) \quad (3)$$

with

$$V_{ij} = \sum_{i < j} \frac{\mu_0}{4\pi} \frac{\gamma_i \gamma_j \hbar^2}{|\mathbf{r}_i - \mathbf{r}_j|^3} \frac{(1 - 3 \cos \beta_{ij})}{2} \quad (4)$$

where  $\mu_0$  is the vacuum permeability,  $\gamma$  is the geomagnetic ratio of the spin,  $\beta_{ij}$  is the angle between the line segment connecting  $(\mathbf{r}_i, \mathbf{r}_j)$  and the direction of the bias external magnetic field (along z-direction in this case). Eq. (3) is able to describe the dipolar interaction for the spin systems with an arbitrary spin number as long as the spin angular momentum operators  $S_\mu$  obey the commutation relation  $[S_i, S_j] = i\epsilon_{ijk}S_k$ . It applies to the spin-1/2 systems we discussed in the main text and Nitrogen-Vacancy (NV) centers which are spin-1 systems.

a. NV ensemble

Here we consider NV ensemble and only  $|m_s = 1\rangle$  and  $|m_s = 0\rangle$  are used as a 2-level system. The spin-1 operators are

$$S_x^{(1)} = \frac{1}{\sqrt{2}} \begin{pmatrix} 0 & 1 & 0 \\ 1 & 0 & 1 \\ 0 & 1 & 0 \end{pmatrix}, S_y^{(1)} = \frac{1}{\sqrt{2}} \begin{pmatrix} 0 & -i & 0 \\ i & 0 & -i \\ 0 & i & 0 \end{pmatrix}, S_z^{(1)} = \begin{pmatrix} 1 & 0 & 0 \\ 0 & 0 & 0 \\ 0 & 0 & -1 \end{pmatrix}. \quad (5)$$

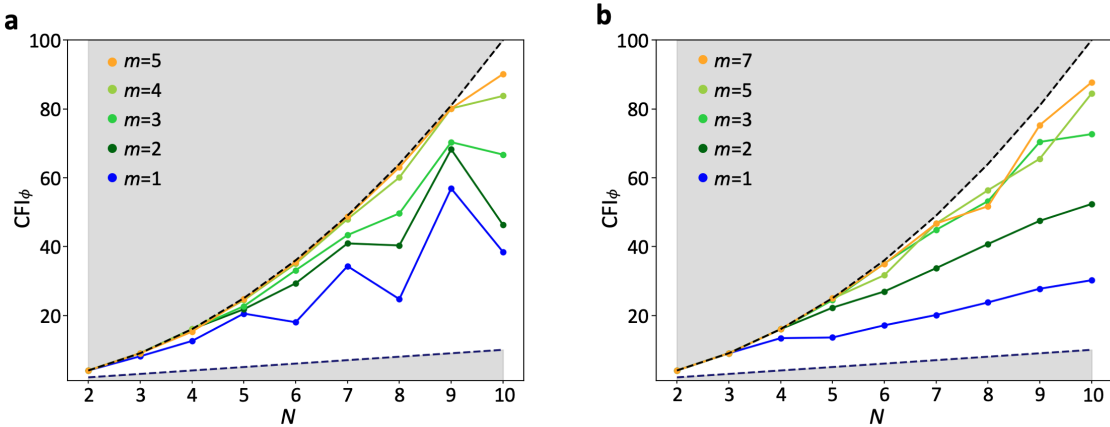
If we only take the  $|m_s = 1\rangle$ ,  $|m_s = 0\rangle$  subspace into consideration, the relations between the ‘truncated’ spin-1 operators and the spin-1/2 operators are:

$$S_y^{(1)} = \sqrt{2}S_y^{(\frac{1}{2})}, S_z^{(1)} = \sqrt{2}S_y^{(\frac{1}{2})}, S_z^{(1)} = \frac{I}{2} + S_x^{(\frac{1}{2})}. \quad (6)$$

Plugging Eq. (6) into Eq. (3), we get the effective dipole-dipole interaction Hamiltonian for NV ensemble  $|m_s = 1\rangle$ ,  $|m_s = 0\rangle$  subspace [2,4]:

$$H_{DD,NV} = \sum_{i < j} V_{ij} (S_{zi}^{(\frac{1}{2})} S_{zj}^{(\frac{1}{2})} - S_{xi}^{(\frac{1}{2})} S_{xj}^{(\frac{1}{2})} - S_{yi}^{(\frac{1}{2})} S_{yj}^{(\frac{1}{2})}). \quad (7)$$

Fig. 2(a) shows the Classical Fisher Information (CFI) optimization results for 2D square lattice spin configuration. They are similar to the results we get in Fig.(2) of the main text for spin-1/2 systems.



**Supplementary Figure 2. Different types of dipolar interactions:** (a) Optimization results for NV-ensemble. The CFI saturates the theoretical upper bound Heisenberg Limit (HL) when the variational circuit layer number goes up from 1 to 7, and the CFI results are ‘oscillating’ for even/odd number of spins from shallow circuit. (b) Optimization results for Ising type spin interaction when there is large local disorder in the system.

b. Ising type interaction (large local disorder)

When the system has large local disorder, the flip-flop terms in the dipolar interaction Hamiltonian Eq. (3) are suppressed because of the large energy gap:

$$\begin{aligned} H_{DD,Ising} &= \sum_i \delta_i S_{zi}^{(\frac{1}{2})} + \sum_{i < j} V_{ij} (2S_{zi}^{(\frac{1}{2})} S_{zj}^{(\frac{1}{2})} - S_{xi}^{(\frac{1}{2})} S_{xj}^{(\frac{1}{2})} - S_{yi}^{(\frac{1}{2})} S_{yj}^{(\frac{1}{2})}) \\ &= \sum_i \delta_i S_{zi}^{(\frac{1}{2})} + \sum_{i < j} 2V_{ij} (S_{zi}^{(\frac{1}{2})} S_{zj}^{(\frac{1}{2})} - S_{+i}^{(\frac{1}{2})} S_{-j}^{(\frac{1}{2})} - S_{-i}^{(\frac{1}{2})} S_{+j}^{(\frac{1}{2})}) \\ &\approx \sum_i \delta_i S_{zi}^{(\frac{1}{2})} + \sum_{i < j} 2V_{ij} S_{zi}^{(\frac{1}{2})} S_{zj}^{(\frac{1}{2})}. \end{aligned} \quad (8)$$

This location-dependent single-spin energy shift ( $\delta_i$ ) can be canceled by spin-echo pulse sequence where the interaction gate  $D(\tau)$  needs to be applied:

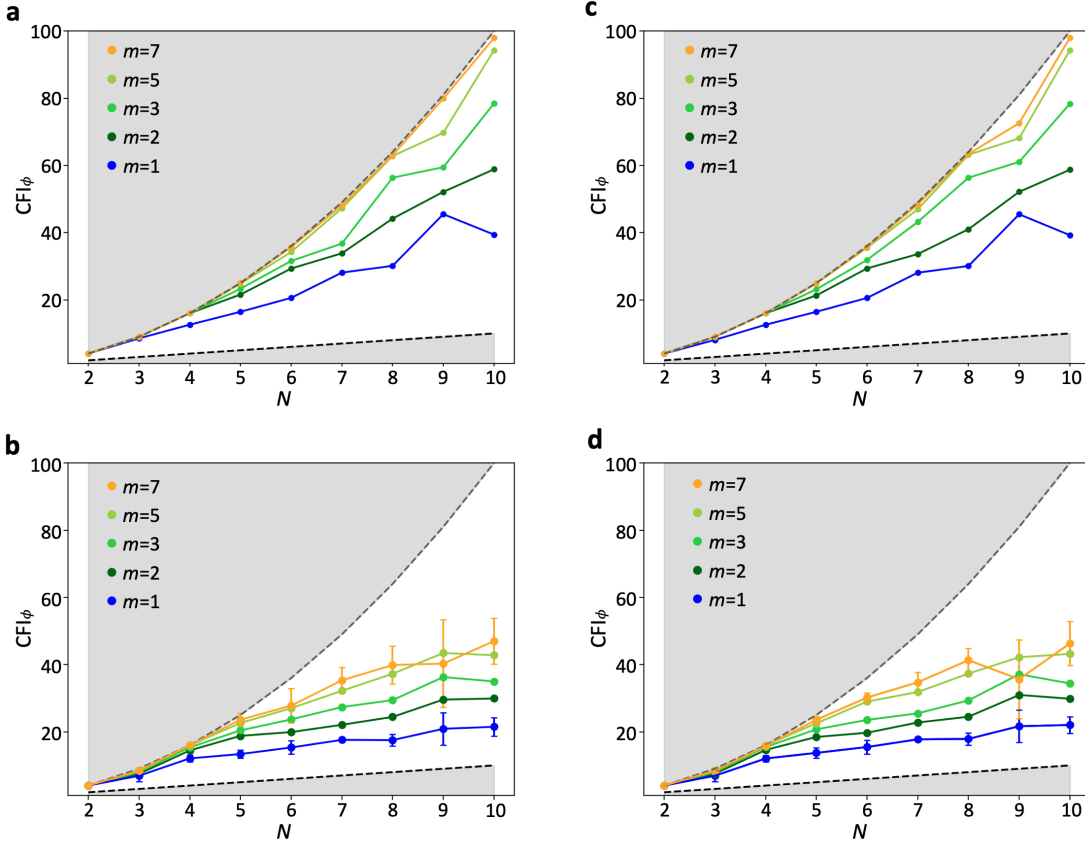
$$\begin{aligned} D(\tau) &= R_x(\pi) \exp[-i\tau H_{\text{DD,Ising}}] R_x(\pi) \exp[-i\tau H_{\text{DD,Ising}}] \\ &= \exp \left[ -i\tau \sum_{i < j} 2V_{ij} S_{zi}^{(\frac{1}{2})} S_{zj}^{(\frac{1}{2})} \right]. \end{aligned} \quad (9)$$

Eq. (9) is also valid when the local disorder  $\delta_i$  is comparable with the interaction strength  $V_{ij}$ . If there is local disorder in the dipolar-interacting spin ensemble, applying spin-echo will generate the interaction gate  $D(\tau)$  where the local disorder terms are canceled.

The CFI optimization results by using the effective Ising type interaction Hamiltonian  $H_{\text{DD,Ising}} = \sum_{i < j} 2V_{ij} S_{zi}^{(\frac{1}{2})} S_{zj}^{(\frac{1}{2})}$  is shown in Fig. 2 (b).

From Fig. 2, the CFI results close to the Heisenberg Limit are observed, indicating that the variational method can be applied to different kinds of spins in solid state systems and generate highly entangled state for high-precision quantum metrology. We also observe that for shallow variational circuits, the CFI ‘oscillation’ between even and odd spin numbers only appears when there are flip-flop terms in the Hamiltonian. For Ising type interaction, the ‘oscillation’ disappears.

**Supplementary Figure 3: Optimization results by using  $P_z^{\text{tot}}$ ,  $P_z^\pi$  as measurement bases**



**Supplementary Figure 3. Optimized CFI with different measurement bases:** (a) 2D square lattice using observable  $P_z^{\text{tot}}$ , (b) 3D-random configuration using observable  $P_z^{\text{tot}}$  (averaged over 5 cases), (c) 2D square lattice using observable  $P_z^\pi$ , (d) 3D-random configuration using observable  $P_z^\pi$  (averaged over 5 cases). All error bars indicate one standard deviation of the CFI from different spin configurations.

The optimization results shown in Fig. 2 in the main text are obtain by using  $P_z$  as the measurement basis for the CFI (cost function) calculation. Although measuring all the diagonal elements in the density matrix of the resulting

states provides the maximum information one can get from single-qubit measurement and a large Hilbert space for the optimizer, it leads to an exponentially large ( $2^N$ ) experimental repetition number when the CFI needs to be estimated from experimental data. Thus, we test the variational method on two other measurement bases which require less repetitions for readout.

The measurement basis on total spin polarization along  $z$ -direction is given by

$$P_z^{\text{tot}} \equiv |J = N/2, J_z\rangle \langle J = N/2, J_z|, \quad (10)$$

where  $J$  is the total spin angular momentum quantum number and  $J_z$  is the total spin angular momentum projection quantum number that runs from  $N/2$  to  $-N/2$ .  $P_z^{\text{tot}}$  has  $N + 1$  outcomes, so it scales linear with the system size.

The optimization results by using the CFI on  $P_z^{\text{tot}}$  as cost function are shown in Fig. 3 (a)(b). Surprisingly, compared to the results by using  $P_z$ , the optimization results from using  $P_z^{\text{tot}}$  are improved by about a factor of 1.3 for the 3D-random spin configuration. Since all the information one can extract from  $P_z^{\text{tot}}$  are contained in  $P_z$ , we attribute this improvement to the simpler parameter space structure that  $P_z^{\text{tot}}$  provides to the optimizer. Less local maximum points in the parameter space will help the optimizer to converge to a high CFI point, especially when the dimension of the parameter space ( $3m$ ) is large.

Parity of the spin ensemble,

$$P_z^\pi \equiv \prod_i^N \sigma_{zi}, \quad (11)$$

provides a constant (2) dimensional outcome space for experimental readout. Improvements are also observed in 2D square lattice and 3D-random spin configurations (Fig. 3(c)(d)).

#### Supplementary Figure 4: Mutual Information of the Metrological States

The Rényi entropy of order  $n$  of a subsystem A is defined as

$$S_n(A) = \frac{1}{1-n} \log \text{Tr}(\rho_A^n) \quad (12)$$

which describes the general entanglement correlation between the subsystem A and the full system [5,6]. In the limit  $n \rightarrow 1$ , the Renyi entanglement entropy approaches the von Neumann entanglement entropy  $E_{\text{vN}} = -\text{Tr}(\rho_A \log \rho_A)$ , which we used to characterize the entanglement of the metrological states in Fig.3 of the main text. The 2-nd order Rényi entropy reflects the purity of the state  $\text{Tr}(\rho_A^2) \leq 1$ . It is an indication of entanglement when the purity of the subsystem is smaller than the purity of the full system [7],  $\text{Tr}(\rho_A^2) < \text{Tr}(\rho_{AB}^2)$ .

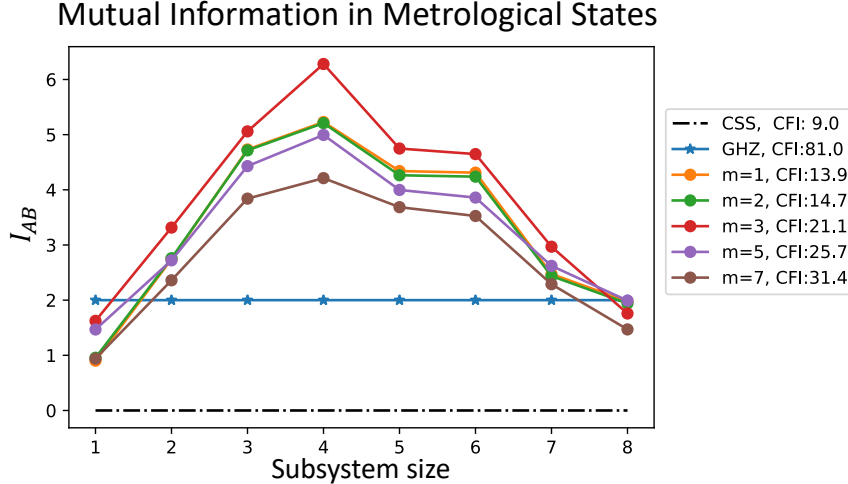
By measuring the 2-nd order Rényi entropy, we can calculate the mutual information between the two subsystems A and B.

$$I_{AB} = S_2(A) + S_2(B) - S_2(AB). \quad (13)$$

The scaling of the mutual information with respect to the subsystem size is one of the keys to study the entanglement properties of interacting quantum systems, e.g. area law and volume law [8,7,9]. Here, we numerically calculate the mutual information of the 9-spin metrological states generated by the variational circuits with different layer numbers.

As shown in Fig. 4, unlike CFI, the mutual information does not monotonically increase with the circuit layer number  $m$ . If entanglement is quantified by mutual information, all the metrological states we studied here have ‘more’ entanglement compared to the GHZ states, even though the CFI are lower. These results reflect that deep entanglement does not necessarily lead to better sensing performance (CFI), global and shallow entanglement is preferred for Heisenberg-limit quantum sensing.

We can understand the relation between CFI and entanglement by taking a 4-qubit GHZ state  $|\text{GHZ}\rangle = \frac{1}{\sqrt{2}}(|0000\rangle + |1111\rangle)$  as an example.  $|\text{GHZ}\rangle$  has the highest CFI. However, there is only 1 ebit of entanglement between the two qubits on the left and the two on the right.  $S_2(A) = S_2(B) = 1, I_{AB} = 2$ . Consider another state  $|\psi\rangle = \frac{1}{2}(|0000\rangle + |1111\rangle + |0101\rangle + |1010\rangle)$ . The amount of entanglement between the left and right two qubits are 2 ebits.  $S_2(A) = S_2(B) = 2, I_{AB} = 4$ . The last two terms in  $|\psi\rangle$  contribute negatively to the CFI of the state, even though they provide more entanglement.

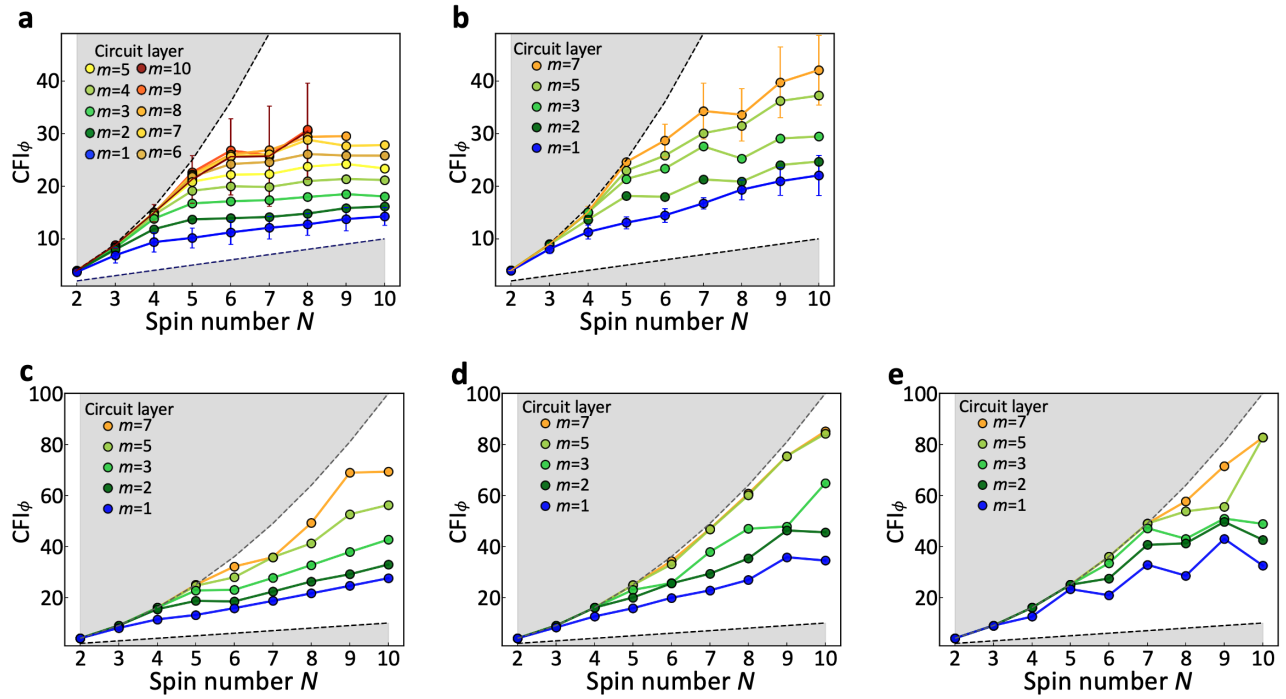


**Supplementary Figure 4. Mutual information versus subsystem size of the 9-spin metrological states:** The spatial spin configuration is the same as Fig.3(b) (case No.2 in 50 random cases) and the  $m = 1\text{--}7$  results are calculated (including the states that shown in Fig.3(b) left/right in the main text). The asymmetry of the mutual information with respect to the subsystem size comes from the random spin locations.

**Supplementary Figure 5: Complete CFI data for Fig.2 in main text**

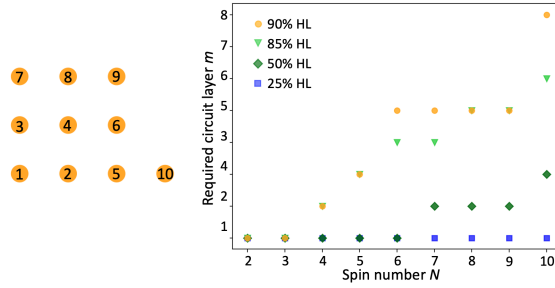
The complete data for dipolar-interacting spin systems' CFI optimization is shown in this section. Fig. 5(a) shows the 50-cases averaged optimization results for 3D-random spin configurations, the variational circuit layer number  $m$  is chosen from 1 to 10. The optimized CFI results are approaching to the Heisenberg Limit (HL) when more layers ( $m$ ) are used. However, when  $m > 7$ , the CFI results stop increasing. This CFI 'saturation' effect might be caused by two reasons. First, when  $m$  is large, the number of the local maximum points in the high dimensional parameter space increases. This could potentially cause the optimizer to stuck in the local maximum point. Sometimes, take  $N = 7, m = 10$  data in Fig. 5(a) as an example, adding more variational layers even leads to a lower CFI optimization result. The 'local maximum' problem could be solved by more advanced and powerful optimization algorithms, such as reinforcement learning [10–12], and more computational resources. Second, the 'saturation' effect reflects the global maximum CFI one can reach, no matter what kind of optimization algorithm is applied. It's still an open question what is the highest CFI the spin ensemble could reach for a given configuration.

Fig. 5(b)-(e) show the CFI optimization result for 2D random (10-cases average), 1D chain, 2D square lattice and 2D symmetric cycle spin configurations. The results of regular patterns are better than those of 2D/3D-random patterns. Due to the angular dependent term ( $1 - 3 \cos^2 \theta$ ) in dipolar interaction, the results from 2D-random spin configuration (Fig. 5(b)) are better than the results from 3D-random patterns (Fig. 5(a)).



**Supplementary Figure 5. The complete CFI data:** (a) 3D random, (b) 2D random, (c) 1D chain, (d) 2D square lattice, and (e) 2D circle. All error bars indicate one standard deviation of the CFI from different spin configurations.

**Supplementary Figure 6: Required layers to reach given CFI for 2D square lattice**



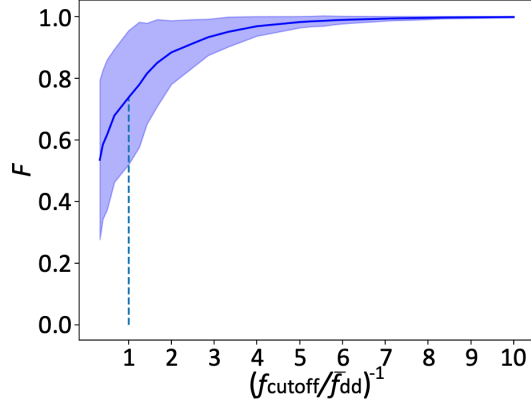
**Supplementary Figure 6. Scalability of 2D square spin lattice:** Left: Schematic of a 2D square lattice pattern. The numbers label the order in which spins are added to form a lattice of size  $N$ . Right: Number of layers required to achieve a CFI within a given percentage of the HL.

As shown by the schematic on the left, the distances between spin No.4 and spin No.5, 7, and 9 are the same, so the interaction strengths between each pair are the same. Similarly, the distance between spin No.4 and spin No.2, 3, 6, and 8 are the same (smaller). Therefore, the plateau features in Fig.(6) are likely due to this symmetry: adding one more spin to the lattice does not require an extra layer to reach a given percentage of the CFI.

**Supplementary Figure 7: Orders of interaction**

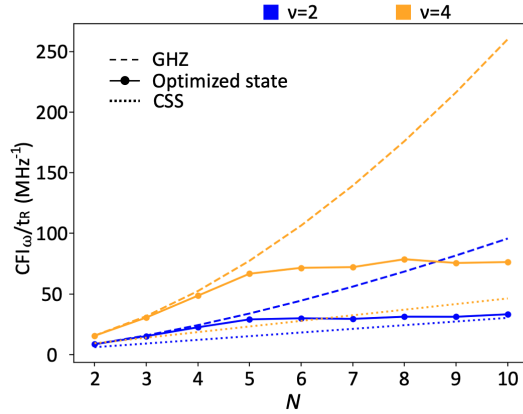
Due to the decaying feature ( $\frac{1}{r^3}$ ) of dipolar interaction strength, the resulting states might be mainly generated by nearest-neighbor interaction. For studying ‘how much’ interaction is essential for generating the resulting entangled states, we calculate the overlap (state fidelity [13]) between the original state and the new state, which is generated

by using the cutoff Hamiltonian and optimized parameters. A cutoff interaction strength  $f_{\text{cutoff}}$  is chosen, and all the pairwise potential  $V_{ij}$  smaller than  $f_{\text{cutoff}}$  are set to zero in the cutoff Hamiltonian. Fig. 7 shows the relation between the state fidelity  $F$  versus  $f_{\text{cutoff}}$ . A state fidelity value less than 1 is observed when  $f_{\text{cutoff}}$  is set to be equal to the averaged nearest-neighbor interaction strength  $f_{dd}$ . This result reflects higher order interactions in the spins ensemble are utilized for the metrological states generation.



**Supplementary Figure 7. Long range interaction for preparing metrological states:** Average state fidelity vs. different cutoff strength in  $H_{dd}$ . The shaded area indicates the standard deviation. Data obtained from 3D-random  $N = 10, m = 5$ , 50-cases optimization results.

**Supplementary Figure 8: Non-Markovian noise sensing performance in 3D random spin configurations**



**Supplementary Figure 8. Sensing performance of 3D random spin configurations:** Average Ramsey protocol's results of the generated entangled states in 3D random configurations when considering non-Markovian noise in the signal accumulation step. Blue and orange correspond to two different noise models ( $\nu = 2$  and  $4$ ).

**Supplementary Figure 9: Optimized states with different readout fidelity**

We run the optimization with imperfect readout for  $N = 4$  and  $N = 10$  2D square lattice spin configurations. The optimized states resemble GHZ states (high RF), SSS (low RF), CSS (RF close to 50%). For  $N = 4$  case, the Gaussian state appears for RF lower than 92%, but for  $N = 10$  case, the Gaussian states appears when RF is about 96%. We expected that for large spin system with finite RF, Gaussian states (e.g. SSS) are advantageous for quantum-enhanced metrology.

<b>a</b> Spin number N = 4:	Wigner Plot								
	RF	1.00	0.99	0.98	0.97	0.96	0.95	0.94	0.93
	CFI	15.27	11.07	9.27	7.83	6.91	6.03	4.81	4.62
	CSS	4.00	3.84	3.67	3.53	3.39	3.24	3.10	2.96
	Wigner Plot								
	RF	0.92	0.91	0.90	0.80	0.70	0.60	0.50	
	CFI	3.83	3.54	3.28	1.56	0.65	0.16	$10^{-32}$	
	CSS	2.82	2.69	2.56	1.44	0.64	0.16	$10^{-33}$	
	Wigner Plot								
<b>b</b> Spin number N = 10:	RF	1.00	0.98	0.96	0.94	0.92			
	CFI	85.18	30.18	18.18	14.34	11.66			
	CSS	10.00	9.216	8.464	7.744	7.056			
	Wigner Plot								
	RF	0.9	0.80	0.70	0.60				
	CFI	9.67	4.166	1.654	0.401				
	CSS	6.40	3.6	1.6	0.4				

**Supplementary Figure 9. Highly entangled state requires high readout fidelity:** Optimized states' Wigner distributions when finite readout fidelity (RF) is assumed in the optimization process. The 'CSS' row reports the CFI value when using the CSS for sensing under same RF.

#### SUPPLEMENTARY TABLES

Supplementary Table 1: Relative experimental parameter table (full)

Supplementary Table 1. Experimental platforms' data

System	$T_2^{(\text{best})}$	$T_2^{(\text{DD})}$	$\bar{f}_{\text{dd}}$	$P_{\text{ini}}$	$F_{\text{readout}}$	$\nu$
NV ensemble	1.58(7)s <sup>a</sup>	7.9(2) $\mu$ s <sup>b</sup>	35kHz <sup>b</sup>	97.5% <sup>c</sup>	97.5% <sup>c</sup>	2 – 4 <sup>b</sup>
P1 centers	0.8ms <sup>e</sup> (DEER)	4.4 $\mu$ s <sup>f</sup>	0.7kHz <sup>e</sup> , 0.92MHz <sup>f</sup>	95% <sup>e</sup>	95% <sup>e</sup>	?
Rare-Earth crystals	$23.2 \pm 0.5$ ms <sup>g</sup>	2.5 $\mu$ s <sup>h</sup>	1.96MHz <sup>h</sup>	97% <sup>i</sup>	94.6% <sup>j</sup>	$2.4 \pm 0.1$ <sup>g</sup>
Cold Molecules	1s <sup>k</sup>	80ms <sup>l</sup>	52Hz <sup>l</sup> , 1.5kHz <sup>m</sup>	97% <sup>m</sup>	97% <sup>m</sup>	?

<sup>a</sup> T.H.Taminiau, NComm 2018, <sup>b</sup> H.Zhou, PRX 2020, <sup>c</sup> M.D.Lukin, PRL 2015, <sup>d</sup> L.Childress Science 2006

<sup>e</sup> T.H.Taminiau, NComm 2021, <sup>f</sup> N.Yao, Nature 2021

<sup>e</sup> P.Bertet, Science advances 2021, <sup>h</sup> A.Reiserer, PRL 2021, <sup>i</sup> J.Thompson, Science 2020, <sup>j</sup> J.Thompson, NComm 2020

<sup>k</sup> M.R Tarbutt PRL 2020, <sup>l</sup> B.Yan, J.Ye, Nature 2013, <sup>m</sup> J Doyle, PRL 2020

Based on the simulation results shown in Fig.4(c) in main text, we need  $\bar{f}_{dd}T_2 \geq 5$  to generate metrological states that beat the SQL. It's worth mentioning that the  $T_2$  in this situation stands for the coherence time *without* the dipole-dipole interaction's influence. During the state preparation step, the dipolar interactions between the spins are included in the system Hamiltonian for the entanglement generation ( $D$  gate in Fig.1(c) in main text). Thus, the  $T_2^{(\text{DD})}$  in Table 1 is a lower bound and  $T_2^{(\text{best})}$  is a more precise estimation for the spin coherence time.

## SUPPLEMENTARY NOTES

### Supplementary Note 1: Designing the variational circuit

In this section, we discuss how to choose the experimentally realizable elementary gates in the variational sequence of the entangler based on limited quantum resource [14, 15].

#### c. Entanglement generation gates from two-body interaction Hamiltonian and global rotations

Consider a two-body interaction Hamiltonian:

$$H_{\text{int}} = \sum_{i < j} V_{ij} (J^I S_{zi} S_{zj} + J^S \mathbf{S}_i \cdot \mathbf{S}_j). \quad (14)$$

In this Hamiltonian,  $\mathbf{S} = (S_x, S_y, S_z)$  is the vector of spin-1/2 operators,  $V_{ij}$  is the interaction strength between spin  $i$  and  $j$  which depends on their locations, and  $J^I (\neq 0)$ ,  $J^S$  are the Ising and symmetric coupling constant respectively.

The elementary gates in each layer of the variational circuit for preparing metrological states (Fig.1(c) main text) include two free evolutions under the interaction Hamiltonian  $D(\tau), D(\tau')$ , one global rotation along the  $x$ -axis  $R_x(\vartheta)$  and two fixed  $\pi/2$  rotations  $R_y(-\frac{\pi}{2}), R_y(\frac{\pi}{2})$  along the  $y$ -axis. We define the interaction gate in the  $z$ -direction as

$$D_z(\tau) \equiv \exp(-i\tau H_{\text{int}}/\hbar) = \exp \left[ -i\tau \sum_{i < j} V_{ij} (J^I S_{zi} S_{zj} + J^S \mathbf{S}_i \cdot \mathbf{S}_j) / \hbar \right]. \quad (15)$$

The interaction gates in other directions can be obtained by  $\pi/2$  rotations:

$$\begin{aligned} D_{x,y}(\tau) &= R_{y,x}(\pi/2) D_z(\tau) R_{y,x}(-\pi/2) \\ &= \exp \left[ -i\tau \sum_{i < j} V_{ij} (J^I S_{x,yi} S_{x,yj} + J^S \mathbf{S}_i \cdot \mathbf{S}_j) / \hbar \right]. \end{aligned} \quad (16)$$

In Eqs. (15) (16), the symmetric interaction term stay unchanged because inner product is conserved under global rotation and the ‘direction of interaction’ is only determined by the Ising term. Using these definitions, we simplify the gate set in each layer as

$$\begin{aligned} \mathcal{U}_i &= R_y \left( \frac{\pi}{2} \right) D(\tau'_i) R_y \left( -\frac{\pi}{2} \right) R_x(\vartheta_i) D(\tau_i) \\ &= D_x(\tau'_i) R_x(\vartheta_i) D_z(\tau_i). \end{aligned} \quad (17)$$

In the next two subsections, it will be shown that the sequence in Eq. (17) is the most general gate set that uses only global rotations and preserves the collective spin direction along  $x$ -direction.

#### d. Preservation of the collective spin direction

Define the  $x$ -parity operator  $P_x \equiv \prod_i^N \sigma_{xi} = P_x^\dagger$ , with  $P_x^2 = I$ . This operator describes the parity of a state in  $x$ -direction and is related to the global  $\pi$  rotation along  $x$ -axis up to a phase constant,  $R_x(\pi) = \exp(-i\pi \sum_i S_{xi}) = (-i)^N \prod_i^N \sigma_{xi}$ . Applying the  $x$ -parity operator onto individual spin’s angular momentum operator gives  $P_x S_{\mu j} P_x = (\sigma_x S_\mu \sigma_x)_j = \pm S_{\mu j}$ . Thus the interaction gates along  $x$ - and  $z$ -direction conserve the  $x$ -parity,  $P_x D_{x,z} P_x = D_{x,z}$ . Similarly, the only global rotation that conserves  $x$ -parity for arbitrary angles is  $R_x(\vartheta)$ . Then, based on Eq.(1) in the main text, the unitary operator of the whole control sequence conserves the  $x$ -parity

$$\begin{aligned} P_x \mathcal{S}(\boldsymbol{\theta}) P_x &= P_x \mathcal{U}_m \dots \mathcal{U}_2 \mathcal{U}_1 P_x \\ &= P_x \prod_i [D_x(\tau'_i) R_x(\vartheta_i) D_z(\tau_i)] P_x \\ &= \mathcal{S}(\boldsymbol{\theta}). \end{aligned} \quad (18)$$

The initial spin state pointing to the  $+x$ -direction is an eigenstate of  $P_x$ :  $P_x |\uparrow_x\rangle^{\otimes N} = |\uparrow_x\rangle^{\otimes N}$ . Thus, any state produced by this variational circuit remains an eigenstate of  $P_x$ :

$$\begin{aligned} P_x |\Psi(\theta)\rangle &= P_x \mathcal{S}(\theta) |\uparrow_x\rangle^{\otimes N} \\ &= P_x \mathcal{S}(\theta) P_x P_x |\uparrow_x\rangle^{\otimes N} \\ &= |\Psi(\theta)\rangle. \end{aligned} \quad (19)$$

Now consider the expectation value of the total spin angular momentum operator  $J_\mu \equiv \sum_i S_{\mu i}$  ( $\mu \in \{x, y, z\}$ ):

$$\begin{aligned} \langle J_{y,z} \rangle &= \langle \Psi(\theta) | J_{y,z} | \Psi(\theta) \rangle \\ &= \langle \Psi(\theta) | P_x P_x J_{y,z} P_x P_x | \Psi(\theta) \rangle \\ &= -\langle J_{y,z} \rangle = 0. \end{aligned} \quad (20)$$

Thus, the collective spin direction  $\langle \mathbf{J} \rangle / |\langle \mathbf{J} \rangle|$  always points along the  $x$ -direction.

#### e. Choosing the most general gate set

To preserve the collective spin direction along  $x$ -axis, the global rotation and interaction gates that can be chosen are  $R_x$ ,  $D_x$ ,  $D_\perp$  where  $D_\perp$  stands for the interaction gates along any direction perpendicular to the  $x$ -direction. Combining  $R_x$  and  $D_z$  can generate any  $D_\perp$ , thus the simplest gate set fulfilling all the requirements is  $D_x R_x D_z$ , as described by Eq.(1) in the main text.

The derivations and results in this section about selecting the variational sequence agree with ref.[14]. However, the interaction Hamiltonian we discuss here is more general. In Eq. (14), when  $J^I = 1, J^S = 0$ , the interaction becomes Ising type interaction which is equivalent to the Rydberg interaction in ref.[14,15]. The Ising interaction can also describe spin systems with large local disorder. The optimization results are shown in the next section. When  $J^I = 3, J^S = -1$ , Eq. (14) becomes the dipolar interaction Hamiltonian between spin-1/2 particles. When  $J^I = 2, J^S = -1$ , it becomes the dipolar interaction Hamiltonian between spin-1 particles (such as NV centers). The simulation results for this case are shown in the next section. When  $J^I = 1, J^S = -1$ , the interaction can describe the dipolar interaction between cold molecules [16].

#### Supplementary Note 2: CFI with respect to angle and frequency

In general, the Classical Fisher Information (CFI) measures the sensitivity of a statistical model to small changes of a parameter  $\theta$  [17, 18]. Let  $Z$  be a random variable and  $P_z(\theta) \equiv P(z|\theta)$  be its probability distribution which depends on  $\theta$ . Let  $\Theta$  be an unbiased estimator of  $\theta$ , i.e.

$$\theta = \langle \Theta \rangle = \sum_z \Theta \cdot P_z(\theta). \quad (21)$$

From Eq. (21) and the fact that the sum of probabilities of all outcomes is 1,

$$1 = \frac{\partial \langle \Theta \rangle}{\partial \theta} = \frac{\partial}{\partial \theta} \sum_z \Theta P_z(\theta), \quad (22)$$

$$0 = \frac{\partial}{\partial \theta} \sum_z P_z(\theta). \quad (23)$$

Subtracting Eq. (23) multiplied by  $\theta$  from Eq. (22), we get

$$\begin{aligned} 1 &= \sum_z (\Theta - \theta) \frac{\partial}{\partial \theta} P_z(\theta) \\ &= \sum_z P_z(\theta) (\Theta - \theta) \frac{1}{P_z(\theta)} \frac{\partial}{\partial \theta} P_z(\theta) \\ &= \langle (\Theta - \theta) \frac{1}{P_z(\theta)} \frac{\partial}{\partial \theta} P_z(\theta) \rangle \\ &= \langle (\Theta - \theta) \frac{\partial}{\partial \theta} \log P_z(\theta) \rangle. \end{aligned} \quad (24)$$

Letting  $X = \Theta - \theta$  and  $Y = \frac{\partial}{\partial \theta} \log P_z(\theta)$ , by the Cauchy-Schwartz inequality for random variables:  $\langle XY \rangle^2 \leq \langle X^2 \rangle \langle Y^2 \rangle$ , we have

$$\langle (\Theta - \theta)^2 \rangle \left\langle \left( \frac{\partial}{\partial \theta} \log P_z(\theta) \right)^2 \right\rangle \geq 1, \quad (25)$$

where

$$\begin{aligned} \langle (\Theta - \theta)^2 \rangle &= \langle \Theta^2 \rangle - (2\theta \langle \Theta \rangle - \langle \theta^2 \rangle) \\ &= \langle \Theta^2 \rangle - (2\theta^2 - \theta^2) \\ &= \langle \Theta^2 \rangle - \langle \Theta \rangle^2 \\ &= \Delta\Theta^2 \end{aligned} \quad (26)$$

is the variance of  $\Theta$ . Define

$$\text{CFI} \equiv \sum_z P_z(\theta) \left( \frac{\partial}{\partial \theta} \log P_z(\theta) \right)^2, \quad (27)$$

we have

$$\Delta\Theta^2 \geq \frac{1}{\text{CFI}}. \quad (28)$$

If the measurement is repeated  $M$  times, then by the additive property of CFI, we obtain the Cramér-Rao bound:

$$\Delta\Theta^2 \geq \frac{1}{M \cdot \text{CFI}}. \quad (29)$$

In our variational circuit, we use CFI with respect to an infinitesimal angle  $\phi$  as the cost function to generate entangled states. In our program, we use a method similar to parameter shift to calculate the  $\text{CFI}_\phi$  of our optimized states [19,20,21]. In the following notation,

1.  $z$  represents a multi-qubit state in the z-basis;
2.  $\mathcal{U}(\phi) = e^{-i\phi J_y}$  is the rotation operator where  $\phi$  is a small angle;
3.  $\psi$  is the state we create from the variational circuit;
4.  $P_z(\theta)$  is the probability of measuring the state  $z$  with the state after rotation.

Then

$$\begin{aligned} \frac{\partial}{\partial \phi} P_z(\phi) \Big|_{\phi \rightarrow 0} &= \frac{\partial}{\partial \phi} |\langle z | \mathcal{U}(\phi) | \psi \rangle|^2 \Big|_{\phi \rightarrow 0} \\ &= \frac{\partial}{\partial \phi} \langle \psi | \mathcal{U}^\dagger(\phi) | z \rangle \langle z | \mathcal{U}(\phi) | \psi \rangle \Big|_{\phi \rightarrow 0} \\ &= \langle \psi | \mathcal{U}^\dagger(\phi) i J_y | z \rangle \langle z | \mathcal{U}(\phi) | \psi \rangle \Big|_{\phi \rightarrow 0} + \langle \psi | \mathcal{U}^\dagger(\phi) | z \rangle \langle z | \mathcal{U}(\phi) (-i) J_y | \psi \rangle \Big|_{\phi \rightarrow 0} \\ &= i \langle \psi | \left( J_y | z \rangle \langle z | - | z \rangle \langle z | J_y \right) | \psi \rangle. \end{aligned} \quad (30)$$

Note that assuming the rotation operator  $\mathcal{U}(\phi) = e^{-i\phi J_y} \equiv \mathcal{U}_y(\phi)$  along  $y$ -axis is for calculation simplicity. In experiments, the signal (e.g. the external B-field) usually induces a rotation along  $z$ -axis,  $\mathcal{U}_z(\phi) = e^{-i\phi J_z}$ . It's equivalent to assume that the prepared state is firstly rotated by a  $R_x(\pi/2)$  pulse and then accumulates a signal  $\phi$  along  $y$ -axis, or firstly accumulates a signal along  $z$ -axis and then rotated by  $R_x(-\pi/2)$  pulse [18]. In another word,  $R_x(-\pi/2)\mathcal{U}_z(\phi) = \mathcal{U}_y(\phi)R_x(\pi/2)$ , so the signal accumulation process we assumed in the calculation is able to simulate the experiments.

After creating the entangled states, we want to know how useful they are in a Ramsey spectroscopy, where the signal we want to detect is a frequency  $\omega$ . By the same calculation as above except the difference that we take derivative with respect to  $\omega = \frac{\phi}{t_R}$  where  $t_R$  is the Ramsey sensing time, we have

$$\text{CFI}_\omega = \text{CFI}_\phi \cdot t_R^2. \quad (31)$$

**Supplementary Note 3: Relation between CFI<sub>ω</sub> and SNR in single qubit Ramsey experiment**

We illustrate the Ramsey protocol for a single qubit.

1. The qubit is initialized into the ground state  $|0\rangle$ .
2. A  $\frac{\pi}{2}$  pulse along the y-direction is applied to transform it into a superposition state  $\frac{1}{\sqrt{2}}(|0\rangle + |1\rangle)$ . Its matrix form is

$$\rho(t) = \frac{1}{2} \begin{pmatrix} 1 & 1 \\ 1 & 1 \end{pmatrix}. \quad (32)$$

3. After evolving under noise and a signal with frequency  $\omega$  for time  $t$ , its state becomes

$$\rho(t) = \frac{1}{2} \begin{pmatrix} 1 & e^{-i\omega t}e^{-2\gamma t} \\ e^{i\omega t}e^{-2\gamma t} & 1 \end{pmatrix} \quad (33)$$

where  $\gamma$  is the decoherence rate.

4. A second  $\frac{\pi}{2}$  pulse along the x-direction is applied for readout. The qubit is then in the state

$$R_x \left( \frac{\pi}{2} \right) \rho(t) R_x^\dagger \left( \frac{\pi}{2} \right) \quad (34)$$

5. After the rotation, the probability of the qubit being in the ground state is

$$P_0 = \frac{1}{2} + \frac{1}{2} e^{-2\gamma t} \sin \omega t. \quad (35)$$

The CFI with respect to  $\omega$  is

$$\text{CFI}_\omega = \frac{1}{P_0} \left( \frac{\partial P_0}{\partial \omega} \right)^2 + \frac{1}{P_1} \left( \frac{\partial P_1}{\partial \omega} \right)^2 = \frac{t^2 \cos^2 \omega t}{e^{4\gamma t} - \sin^2 \omega t}. \quad (36)$$

Assuming only quantum projection noise, the Signal-to-Noise Ratio (SNR) is  $\frac{\delta P_0}{\sqrt{\frac{1}{M} P_0(1-P_0)}}$  where  $M$  is the total number of measurements. Then

$$\text{SNR}^2 = \frac{M t^2 \cos^2 \omega t \delta \omega^2}{e^{4\gamma t} - \sin^2 \omega t}. \quad (37)$$

Assuming no time overhead, i.e.,  $M = \frac{T_{\text{tot}}}{t_R}$  where  $T_{\text{tot}}$  is the total measurement time and  $t_R$  is the time between Ramsey pulses, we obtain the relationship

$$\text{CFI}_\omega \cdot \frac{T_{\text{tot}}}{t_R} \cdot \delta \omega^2 = \text{SNR}^2. \quad (38)$$

In unit time ( $T_{\text{tot}} = 1\text{s}$ ), when  $\text{SNR} = 1$ , the smallest signal we can measure is

$$\delta \omega = \frac{1}{\sqrt{M \cdot \text{CFI}_\omega}}, \quad (39)$$

leading to the saturated Cramér-Rao bound.

#### Supplementary Note 4: Maximum Likelihood Estimator

Since a measurement collapses a quantum state to an eigenstate of the observable, it's impossible to directly measure  $P(\theta)$ . In experiments, we repeat the sequence to obtain the results for estimating the  $P(\theta)$  and then get an estimate value of  $\theta$ . To understand the relation between the variance of the estimation and CFI, we introduce the Maximum Likelihood Estimator (MLE), which has asymptotic properties to saturate the Cramér-Rao bound. An experimental implementation of MLE to estimate the phase shift of an entangled four-photon Dicke state is given in [22]. A proof that MLE is an unbiased estimator which asymptotically saturates the Cramér-Rao bound is given in [23]. We summarize the proof below.

Let  $\mathbf{X} = \{X_1, X_2, \dots, X_M\}$  be a collection of independent and identically distributed (i.i.d.) random variables with a parametric family of probability distributions  $\{P(X|\theta) | \theta \in \Theta\}$ , where  $\theta$  is an unknown parameter and  $\Theta$  is the parameter space. Let  $\mathbf{x} = \{x_1, x_2, \dots, x_M | x_i \in X_i\}$  be the experimental data set from  $M$  repetitions. The goal is to estimate  $\theta$  (the signal we want to measure) from  $\mathbf{x}$ , i.e., find  $\theta$  that is most likely to produce the outcome  $\mathbf{x}$ . Thus, the normalized log-likelihood function is defined as

$$L_M(\theta) = \frac{1}{M} \log P(\mathbf{X}|\theta) = \frac{1}{M} \log \prod_{i=1}^M P(X_i|\theta) = \frac{1}{M} \sum_{i=1}^M \log P(X_i|\theta). \quad (40)$$

A MLE maximizes the log-likelihood function

$$\Theta_{\text{MLE}} = \underset{\theta \in \Theta}{\operatorname{argmax}} L_M(\theta). \quad (41)$$

In the following, we first show that

1.  $\Theta_{\text{MLE}}$  converges to the true parameter  $\theta_0$ ;
2. the distribution of  $\sqrt{M}(\Theta_{\text{MLE}} - \theta_0)$  tends to a normal distribution  $\mathcal{N}\left(0, \frac{1}{\text{CFI}_{\theta_0}}\right)$  as  $M$  increases.

In other words, not only does the MLE converge to the true parameter, it converges at a rate  $\frac{1}{\sqrt{M}}$ .

Define

$$L(\theta) = \langle \log P(\mathbf{X}|\theta) \rangle_{\theta_0} \quad (42)$$

which denotes the expected log-likelihood function with respect to  $\theta_0$ , then by the Weak Law of Large Numbers (WLLN), the average outcomes from a large number of trials should approach the expected value:

$$\forall \theta, L_M(\theta) \xrightarrow{M \rightarrow \infty} L(\theta). \quad (43)$$

In fact,  $\theta_0$  maximizes  $L(\theta)$ :

$$\begin{aligned} \forall \theta, L(\theta) - L(\theta_0) &= \langle \log P(\mathbf{X}|\theta) \rangle_{\theta_0} - \langle \log P(\mathbf{X}|\theta_0) \rangle_{\theta_0} \\ &= \left\langle \log \frac{P(\mathbf{X}|\theta)}{P(\mathbf{X}|\theta_0)} \right\rangle_{\theta_0} \\ &\leq \left\langle \frac{P(\mathbf{X}|\theta)}{P(\mathbf{X}|\theta_0)} - 1 \right\rangle_{\theta_0} \\ &= \sum_{\mathbf{x} \in \mathbf{X}} \left( \frac{P(\mathbf{x}|\theta)}{P(\mathbf{x}|\theta_0)} - 1 \right) P(\mathbf{x}|\theta_0) \\ &= 1 - 1 = 0. \end{aligned} \quad (44)$$

Moreover, we show that  $\theta_0$  is the unique maximizer. Jensen's inequality states that for a strictly convex function  $f$  and a random variable  $Y$ ,

$$\langle f(Y) \rangle > f(\langle Y \rangle). \quad (45)$$

Taking  $f(y) = -\log y$  and  $P(\mathbf{X}|\theta) \neq P(\mathbf{X}|\theta_0)$ , we have

$$\left\langle -\log \frac{P(\mathbf{X}|\theta)}{P(\mathbf{X}|\theta_0)} \right\rangle_{\theta_0} > -\log \left\langle \frac{P(\mathbf{X}|\theta)}{P(\mathbf{X}|\theta_0)} \right\rangle_{\theta_0} = 0, \quad (46)$$

or

$$L(\theta_0) > L(\theta). \quad (47)$$

Therefore, since

1.  $\Theta_{\text{MLE}}$  maximizes  $L_M(\theta)$ ,
2.  $\theta_0$  maximizes  $L(\theta)$ , and
3.  $L_M(\theta) \xrightarrow{M \rightarrow \infty} L(\theta)$ ,

$\Theta_{\text{MLE}}$  converges to  $\theta_0$ .

Now we use this property to prove that the distribution of  $\Theta_{\text{MLE}}$  tends to the desired normal distribution, where we will apply the Central Limit Theorem (CLT): Suppose  $\mathbf{X} = \{X_1, \dots, X_M\}$  is a sequence of i.i.d. random variables with  $\langle X_i \rangle = \mu$  and  $\text{Var}(X_i) = \sigma^2 < \infty$ . Then as  $M \rightarrow \infty$ , the random variable  $\sqrt{M}(\bar{\mathbf{X}} - \mu)$  converges in distribution to a normal  $\mathcal{N}(0, \sigma^2)$ .

We start with the Mean Value Theorem for the function  $L'_M$ , the derivative of  $L_M$  (continuous by assumption), on the interval  $[\Theta_{\text{MLE}}, \theta_0]$ :

$$\begin{aligned} 0 &= L'_M(\Theta_{\text{MLE}}) = L'_M(\theta_0) + L''_M(\theta_1)(\theta_0 - \Theta_{\text{MLE}}) \\ &\implies \theta_0 - \Theta_{\text{MLE}} = -\frac{L'_M(\theta_0)}{L''_M(\theta_1)} \\ &\implies \sqrt{M}(\theta_0 - \Theta_{\text{MLE}}) = -\sqrt{M} \frac{L'_M(\theta_0)}{L''_M(\theta_1)} \end{aligned} \quad (48)$$

for some  $\theta_1 \in [\Theta_{\text{MLE}}, \theta_0]$ . We analyze the numerator and denominator respectively. The numerator

$$\begin{aligned} L'_M(\theta_0) &= \frac{1}{M} \sum_{i=1}^M (\log P(X_i | \theta_0))' \\ &= \frac{1}{M} \sum_{i=1}^M (\log P(X_i | \theta_0))' - L'(\theta_0) \\ &= \frac{1}{M} \sum_{i=1}^M (\log P(X_i | \theta_0))' - \langle (\log P(\mathbf{X} | \theta_0))' \rangle_{\theta_0} \\ &= \frac{1}{M} \left( \sum_{i=1}^M \log P(X_i | \theta_0) \right)' - \langle (\log P(X_i | \theta_0))' \rangle_{\theta_0} \end{aligned} \quad (49)$$

where the last equality is obtained from the linearity of expected value and derivative. By the CLT, the distribution of  $\sqrt{M}L'_M(\theta_0)$  converges to

$$\mathcal{N}\left(0, \text{Var}_{\theta_0}(\log P(X_i | \theta_0))'\right) \quad (50)$$

where the variance

$$\begin{aligned} \text{Var}_{\theta_0}(\log P(X_i | \theta_0))' &= \langle [(\log P(X_i | \theta_0))']^2 \rangle_{\theta_0} - \langle (\log P(X_i | \theta_0))' \rangle_{\theta_0}^2 \\ &= \sum_{x \in X_1} P(x | \theta_0) \left( \frac{P'(x | \theta_0)}{P(x | \theta_0)} \right)^2 - (L'(\theta_0))^2 \\ &= \text{CFI}_{\theta_0} \end{aligned} \quad (51)$$

by the definition of CFI and that  $\theta_0$  maximizes  $L(\theta)$ . By the consistency property,  $\Theta_{\text{MLE}}$  converges to  $\theta_0$ , and thus  $\theta_1$  converges to  $\theta_0$ . The denominator

$$L''_M(\theta_1) \rightarrow L''_M(\theta_0) = \frac{1}{M} \sum_{i=1}^M [\log P(X_i | \theta_0)]'' \rightarrow \langle [\log P(X_i | \theta_0)]'' \rangle_{\theta_0} \quad (52)$$

by the WLLN. We further show that Eq. (52) is in fact the additive inverse of CFI:

$$\begin{aligned}
\langle [\log P(X_1|\theta_0)]'' \rangle_{\theta_0} &= \left\langle \frac{\partial^2}{\partial \theta^2} \log P(X_1|\theta_0) \right\rangle_{\theta_0} \\
&= \sum_{x \in X_1} [\log P(x|\theta_0)]'' P(x|\theta_0) \\
&= \sum_{x \in X_1} \left( \frac{P''(x|\theta_0)}{P(x|\theta_0)} - \left( \frac{P'(x|\theta_0)}{P(x|\theta_0)} \right)^2 \right) P(x|\theta_0) \\
&= \sum_{x \in X_1} P''(x|\theta_0) - \sum_{x \in X_1} \frac{(P'(x|\theta_0))^2}{P(x|\theta_0)} \\
&= 0 - \text{CFI}_{\theta_0} = -\text{CFI}_{\theta_0}.
\end{aligned} \tag{53}$$

Finally, Eq. (48) becomes

$$\begin{aligned}
\sqrt{M}(\theta_0 - \Theta_{\text{MLE}}) &\xrightarrow{p} \mathcal{N}\left(0, \frac{\text{CFI}_{\theta_0}}{\text{CFI}_{\theta_0}^2}\right) = \mathcal{N}\left(0, \frac{1}{\text{CFI}_{\theta_0}}\right) \\
\implies \Theta_{\text{MLE}} &\xrightarrow{p} \mathcal{N}\left(\theta_0, \frac{1}{M \cdot \text{CFI}_{\theta_0}}\right)
\end{aligned} \tag{54}$$

Thus, the MLE is unbiased and asymptotically saturates the Cramér-Rao bound.

#### Supplementary Note 5: Master equation for a non-Markovian environment

To simulate the performance of our optimized states during the Ramsey measurement with non-Markovian noise, we use a time-local master equation given by [24]. A brief summary of the derivation is given below.

1. The time evolution of a state  $\rho$  is described by

$$\rho(t) = \Lambda(t)[\rho(0)], \tag{55}$$

where  $\Lambda(t)$  includes both the dissipative part and the unitary encoding part. Since  $\Lambda(t)$  is a physical operator that maps a density matrix to a density matrix, it must preserve Hermicity, unit trace, and positivity. Moreover, any quantum state  $\rho$  can be extended by an ancilla to a state  $\rho \otimes \sigma$  of a larger system. The corresponding map  $\Lambda \otimes 1$  must also be positive. This property is known as complete positivity [25]. Thus,  $\Lambda(t)$  is a completely positive and trace preserving (CPTP) linear map.

2. Define the action of  $\Lambda$ . Let  $\mathcal{L}(\mathbb{C}^d)$  be the Hilbert space of linear operators acting on  $\mathbb{C}^d$ , where the inner product is defined as  $\langle \sigma, \tau \rangle = \text{Tr}(\sigma^\dagger \tau)$  (the Hilbert-Schmidt inner product). Let  $\mathcal{LL}(\mathbb{C}^d)$  be the Hilbert space of linear operators acting on  $\mathcal{L}(\mathbb{C}^d)$  which has dimension  $d^2 \times d^2$ . Let  $\{l_i\}_{i=1,\dots,d^2}$  be an orthonormal basis of  $\mathcal{L}(\mathbb{C}^d)$ . Then the action of  $\Lambda \in \mathcal{LL}(\mathbb{C}^d)$  on  $\tau \in \mathcal{L}(\mathbb{C}^d)$  can be expressed as

$$\begin{aligned}
\Lambda[\tau] &= \sum_{i,j=1}^{d^2} \langle l_i, \Lambda[l_j] \rangle \langle l_j, \tau \rangle l_i \\
&\equiv (\Lambda b)^T l
\end{aligned} \tag{56}$$

where the matrix  $\Lambda$  has elements

$$\Lambda_{ij} \equiv \langle l_i, \Lambda[l_j] \rangle \tag{57}$$

and  $b$  is a vector with entries  $b_j = \langle l_j, \tau \rangle$ . Thus,  $\Lambda$  has a unique correspondence with the matrix  $\Lambda$ .

3.  $\Lambda \in \mathcal{LL}(\mathbb{C}^d)$  is trace- and hermicity-preserving if and only if its matrix representation  $\Lambda$  can be written as

$$\begin{pmatrix} 1 & \mathbf{0} \\ \mathbf{m} & \mathbf{M} \end{pmatrix}, \tag{58}$$

where  $\mathbf{0}$  is the zero row vector of length  $d^2 - 1$ ,  $\mathbf{m}$  is a real column vector of length  $d^2 - 1$ , and  $\mathbf{M}$  is a  $(d^2 - 1)(d^2 - 1)$  real matrix.

4. For a single qubit, any operator  $\rho$  on  $\mathbb{C}^2$  can be written as

$$\rho = \frac{1}{2}(\mathbf{I} + \mathbf{v} \cdot \boldsymbol{\sigma}) \quad (59)$$

where  $\mathbf{v}$  is a three-dimensional real vector and  $\boldsymbol{\sigma}$  is the vector of Pauli matrices. Then a map  $\Lambda$  whose matrix representation is given by Eq. (58) acting on  $\rho$  gives

$$\Lambda[\rho] = \frac{1}{2}(\mathbf{I} + (\mathbf{m} + \mathbf{M}\mathbf{v}) \cdot \boldsymbol{\sigma}). \quad (60)$$

5. The Nakajima—Zwanzig projection operator technique can be used to describe non-Markovian behavior [26]. The basic idea of the technique is that the operation of tracing over the environment is regarded as a projection  $\rho_C \rightarrow P\rho_C$  where  $\rho$  is the composite state and  $P$  is a projection operator. The technique makes use of some fairly general assumptions and gives

$$\frac{d}{dt}\rho(t) = \int_0^t K(t,s)\rho(s)ds \quad (61)$$

where  $K(t,s)$  is a memory kernel.

6. Applying Eq. (55) to Eq. (61) gives [27]

$$\begin{aligned} \frac{d}{dt}\rho(t) &= \int_0^t (K(t,s) \circ \Lambda(s))\rho(0)ds \\ &= \int_0^t (K(t,s) \circ \Lambda(s) \circ \Lambda(t)^{-1})\Lambda(t)[\rho(0)]ds \\ &\equiv \Xi(t)\rho(t), \end{aligned} \quad (62)$$

which is of time-local form.

7. Both  $\Lambda(\rho)$  and  $\Xi(\rho)$  can be expanded in the form of Eq. (56):

$$\rho(t) = \Lambda(t)[\rho(0)] = [\Lambda(t)\mathbf{b}(0)]^T l, \quad (63)$$

$$\frac{d}{dt}\rho(t) = \Xi(t)[\rho(t)] = [\Xi(t)\mathbf{b}(t)]^T l. \quad (64)$$

Then

$$\frac{d}{dt}\rho(t) = \left[ \frac{d}{dt}\Lambda(t)\mathbf{b}(0) \right]^T l = [\Xi(t)\Lambda(t)\mathbf{b}(0)]^T l. \quad (65)$$

The corresponding matrix relation is

$$\frac{d}{dt}\Lambda(t) = \Xi(t)\Lambda(t). \quad (66)$$

Equivalently,

$$\Xi(t) = \frac{d\Lambda(t)}{dt}\Lambda(t)^{-1}. \quad (67)$$

8. Assume the noise to be independent, identical, and phase covariant, so that each qubit is described by a map  $\Lambda(t) = \mathcal{U}(t) \circ \Gamma(t)$  and that the uncorrelated noise commutes with signal accumulation [24,28]. Consider the evolution of one qubit described by  $\Lambda(t) = \mathcal{U}(t) \circ \Gamma(t)$ .  $\mathcal{U}(t)$  is defined as

$$\mathcal{U}(t)[\rho(0)] \equiv U(t)\rho(0)U^\dagger(t) \quad (68)$$

where  $U(t) = e^{-i\frac{\omega t}{2}\sigma_z}$  represents the signal accumulation. By Eq. (56) and Eq. (68), the matrix representation of  $\mathcal{U}(t)$  is

$$\mathcal{U}(t) = \begin{pmatrix} 1 & 0 & 0 & 0 \\ 0 & \cos \omega t & -\sin \omega t & 0 \\ 0 & \sin \omega t & \cos \omega t & 0 \\ 0 & 0 & 0 & 1 \end{pmatrix}. \quad (69)$$

$\Gamma(t)$  represents the noise which is trace- and hermiticity- preserving, i.e., has the form in Eq. (58).

9. Solving the commutation relation that gives phase covariant qubit map [24,28]

$$[\mathcal{U}(t), \Gamma(t)] = 0 \iff [\mathbf{U}(t), \Gamma(t)] = 0, \quad (70)$$

we obtain the matrix representation of  $\Gamma(t)$ :

$$\Gamma(t) = \begin{pmatrix} 1 & 0 & 0 & 0 \\ 0 & \eta_{\perp}(t) \cos \theta & -\eta_{\perp}(t) \sin \theta & 0 \\ 0 & \eta_{\perp}(t) \sin \theta & \eta_{\perp}(t) \cos \theta & 0 \\ \kappa(t) & 0 & 0 & \eta_{\parallel}(t) \end{pmatrix}, \quad (71)$$

where  $\mathbf{m} = (0, 0, \kappa(t))^T$  describes a translation along the  $z$ -axis, and  $\mathbf{M} = \begin{pmatrix} \eta_{\perp}(t) \cos \theta & -\eta_{\perp}(t) \sin \theta & 0 \\ \eta_{\perp}(t) \sin \theta & \eta_{\perp}(t) \cos \theta & 0 \\ 0 & 0 & \eta_{\parallel}(t) \end{pmatrix}$  describes a rotation along the  $z$ -axis and a contraction characterized by  $\eta_{\perp}$  and  $\eta_{\parallel}$ . The product of  $\mathbf{U}(t)$  and  $\Gamma(t)$  then gives  $\Lambda(t)$ :

$$\Lambda(t) = \begin{pmatrix} 1 & 0 & 0 & 0 \\ 0 & \eta_{\perp}(t) \cos \phi & -\eta_{\perp}(t) \sin \phi & 0 \\ 0 & \eta_{\perp}(t) \sin \phi & \eta_{\perp}(t) \cos \phi & 0 \\ \kappa(t) & 0 & 0 & \eta_{\parallel}(t) \end{pmatrix} \quad (72)$$

where  $\phi = \omega t + \theta$ .

10. By Eq. (67), we obtain the time-local master equation for a single qubit:

$$\begin{aligned} \Xi(t)[\rho(t)] = & -\frac{i}{2}\omega[\sigma_z, \rho(t)] \\ & + \gamma_+(t)(\sigma_+\rho(t)\sigma_- - \frac{1}{2}\{\sigma_-\sigma_+, \rho(t)\}) \\ & + \gamma_-(t)(\sigma_-\rho(t)\sigma_+ - \frac{1}{2}\{\sigma_+\sigma_-, \rho(t)\}) \\ & + \gamma_z(t)(\sigma_z\rho(t)\sigma_z - \rho(t)), \end{aligned} \quad (73)$$

where

$$\gamma_+(t) = \frac{1}{2} \left( \kappa'(t) - \frac{\eta'_{\parallel}(t)}{\eta_{\parallel}(t)}(\kappa(t) + 1) \right), \quad (74)$$

$$\gamma_-(t) = -\frac{1}{2} \left( \kappa'(t) + \frac{\eta'_{\parallel}(t)}{\eta_{\parallel}(t)}(1 - \kappa(t)) \right), \quad (75)$$

$$\gamma_z(t) = \frac{1}{4} \left( \frac{\eta'_{\parallel}(t)}{\eta_{\parallel}(t)} - 2\frac{\eta'_{\perp}(t)}{\eta_{\perp}(t)} \right). \quad (76)$$

Considering only  $T_2$  noise,  $\gamma_-(t) = \gamma_+(t) = 0$ ,  $\eta_{\parallel}$  is constant, and

$$\eta_{\perp}(t) = e^{-(\frac{t}{T_2})^{\nu}}, \quad (77)$$

where  $\nu$  is the stretch character which equals 1 for Markovian noise. Then

$$\gamma_z(t) = \frac{\nu}{2} \frac{t^{\nu-1}}{T_2^{\nu}}. \quad (78)$$

We further need to express  $\Xi(t)$  as a superoperator acting on the vectorization of  $\rho(t)$ . Defining the vectorization of a matrix as the map

$$\rho = \sum_{i,j} \rho_{ij} |i\rangle \langle j| \mapsto |\rho\rangle = \sum_{i,j} \rho_{ij} |j\rangle \otimes |i\rangle. \quad (79)$$

Define the left and right multiplication superoperators by  $\mathcal{L}(A)[\rho] = A\rho$  and  $\mathcal{R}(A)[\rho] = \rho A$  so that  $[A, \rho] = \mathcal{L}(A)[\rho] - \mathcal{R}(A)[\rho]$ . By this definition, we can calculate the matrix representation  $\mathcal{L}(A) = I \otimes A$  and  $\mathcal{R}(A) = A^T \otimes I$ . Using the superoperator notation, we can express  $\Xi(t)$  as

$$\Xi(t) = -\frac{i}{2}\omega(I \otimes \sigma_z - \sigma_z \otimes I) + \gamma_z(t)(\sigma_z \otimes \sigma_z - I \otimes I). \quad (80)$$

With this expression, we numerically simulate the evolution of our entangled states under non-Markovian noise by using the Time-Dependent Master Equation Solver in QuTip [29].

#### Supplementary Note 6: Performance of metrological states in a non-Markovian environment

To calculate the derivative of probability with respect to  $\omega$  in the calculation for  $\text{CFI}_\omega$ , we use a method similar to parameter shift that utilizes the property that the signal accumulation operator ( $\mathcal{U}(\omega) = e^{-i\omega t J_z}$ ) and the noisy operator commutes. In the following notation,

1.  $z$  represents a multi-qubit state in the  $z$  basis;
2.  $\mathcal{U}(\omega)$  is the effective signal accumulation operator:  $\mathcal{U}(\omega) = e^{-i\omega t J_y}$ ;
3.  $\rho$  is the state density matrix of our optimized state after the noisy evolution without signal for some Ramsey time and a  $\frac{\pi}{2}$  pulse along the  $x$  direction (here we switch the order of the signal accumulation and the second pulse of the Ramsey protocol [18]);
4.  $P(z|\omega)$  is the probability of measuring the state  $z$  with our rotated optimized state after the noisy evolution and signal accumulation.

Then

$$\begin{aligned} \frac{\partial}{\partial \omega} P(z|\omega) \Big|_{\omega \rightarrow 0} &= \frac{\partial}{\partial \omega} \text{Tr}[|z\rangle \langle z| \mathcal{U}(\omega) \rho \mathcal{U}^\dagger(\omega)] \Big|_{\omega \rightarrow 0} \\ &= \frac{\partial}{\partial \omega} \text{Tr}[\mathcal{U}^\dagger(\omega) |z\rangle \langle z| \mathcal{U}(\omega) \rho] \Big|_{\omega \rightarrow 0} \\ &= \text{Tr}\left[\frac{\partial}{\partial \omega} \mathcal{U}^\dagger(\omega) |z\rangle \langle z| \mathcal{U}(\omega) \rho\right] \Big|_{\omega \rightarrow 0} + \text{Tr}[\mathcal{U}^\dagger(\omega) |z\rangle \langle z| \frac{\partial}{\partial \omega} \mathcal{U}(\omega) \rho] \Big|_{\omega \rightarrow 0} \\ &= i t \text{Tr}[(J_y |z\rangle \langle z| - |z\rangle \langle z| J_y) \rho]. \end{aligned} \quad (81)$$

From Eq. (38), since  $T_{\text{tot}}$  and  $\delta\omega^2$  are constants, SNR is proportional to  $\sqrt{\frac{\text{CFI}_\omega}{t_R}}$ . Thus we choose  $\frac{\text{CFI}_\omega}{t_R}$  as the result we show in Fig.4(d) in the main text.

#### Supplementary Note 7: Time Overhead

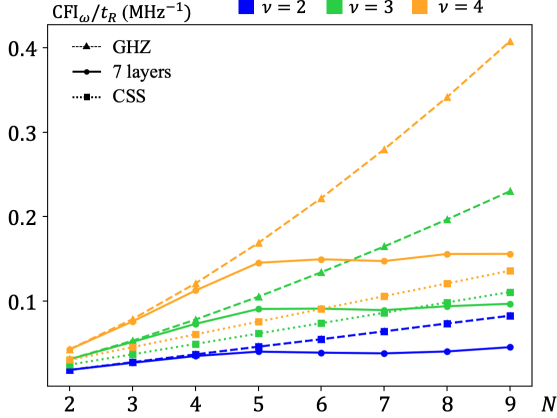
In experiments, the time overhead, including the state preparation and readout time, reduces the repetition number of the sensing sequence and thus decreases the sensitivity. For all the proposed experimental platforms the readout time exceeds the typical  $T_2$  and state preparation time, which means that even for protocols with CSS the time overhead is significant [30].

If we consider a nonzero time overhead, i.e.,  $M = \frac{T_{\text{tot}}}{t_R + t_{\text{oh}}}$ , the expression for  $\text{SNR}^2$  for an uncorrelated spin state becomes

$$\text{SNR}^2 = \frac{T_{\text{tot}} t_R^2 \cos^2(\omega t_R) \delta\omega^2}{(t_R + t_{\text{oh}}) \left( e^{2\left(\frac{t_R}{T_2}\right)^\nu} - \sin^2(\omega t_R) \right)}. \quad (82)$$

If  $t_{\text{oh}} \gg t_R$ , we ignore the term  $t_R$  in the denominator and

$$\text{SNR}^2 \propto \frac{t_R^2}{e^{2\left(\frac{t_R}{T_2}\right)^\nu}}. \quad (83)$$



**Supplementary Figure 10. Sensing performance under large time overhead:** 50 cases average sensing performance of the optimized states when using 7-layer circuit on 3D random spin configuration.

Taking the derivative of Eq. (83) with respect to  $t_R$  gives us the best  $t_R$  if the time overhead is significantly larger:

$$t_R = \frac{T_2}{\nu^{\frac{1}{\nu}}}. \quad (84)$$

Similarly, the same calculations for a GHZ state where the decay term in Eq. (82) becomes  $e^{2n\left(\frac{t_R}{T_2}\right)^\nu}$  show that the best Ramsey sensing time is

$$t_R = \frac{T_2}{(n\nu)^{\frac{2}{\nu}}}. \quad (85)$$

Plugging Eq. (84) and Eq. (85) into Eq. (83), we find that the ratio of the SNR<sup>2</sup> of a GHZ state to that of an uncorrelated spin state is  $n^{1-\frac{2}{\nu}}$ . Thus, only when

$$\nu > 2 \quad (86)$$

do GHZ states provide an advantage in SNR over uncorrelated spin states when  $t_{\text{oh}} \gg t_R$ . We compare the SNR of the states generated by the optimizer with that of the CSS and GHZ states when  $\nu = 2, 3, 4$ . Fig. 10 shows that when we assume a long time overhead, the generated entangled states are less sensitive than CSS when  $\nu = 2$  and  $\nu = 3$  for large spin numbers.

#### Supplementary Note 8: State preparation time comparing to adiabatic method

State preparation time is one of the major components of the time overhead in the generalized Ramsey sensing sequence which influences the sensitivity. The state preparation time of the variational method depends on the circuit layer number  $m$ , system size  $N$  and is proportional to the inverse of average interaction strength  $1/\bar{f}_{\text{dd}}$ . The adiabatic method [31] is an alternative approach to generate entangled states for quantum metrology in dipolar-interacting spin systems by only using single-qubit rotations (global pulses).

To compare the performance of our variational method with the adiabatic method, we derive the relation between the squeezing parameter (Wineland parameter [32]) and CFI. Without loss of generality, we consider a SSS with collective spin direction  $+x$  and is squeezed along the  $y$ -axis (such as the 3rd Wigner distribution shown in Fig. 9(b)). In this case, the squeezing parameter is

$$\xi^2 = N \frac{(\Delta J_y)^2}{|\langle J_x \rangle|^2}, \quad (87)$$

where  $(\Delta O)^2 \equiv \langle O^2 \rangle - \langle O \rangle^2$  and  $N$  is the number of spins. According to the uncertainty principle,

$$(\Delta J_y)^2 (\Delta J_z)^2 \geq \frac{1}{4} |\langle J_x \rangle|^2. \quad (88)$$

The relation between the squeezing parameter and total spin angular momentum uncertainty projection in  $z$ -direction is

$$4(\Delta J_z)^2 \geq \frac{|\langle J_x \rangle|^2}{(\Delta J_y)^2} = N/\xi^2. \quad (89)$$

It's been proven that for a pure Gaussian state, the quantum Fisher information (QFI) is directly related to the variance of the projected spin angular momentum [17,33,34]:

$$\text{QFI} = 4(\Delta J_z)^2. \quad (90)$$

Combining Eq. (89) and Eq. (90), we obtain the relation between CFI and squeezing parameter of a SSS:

$$\text{CFI} \leq \text{QFI} \geq N/\xi^2. \quad (91)$$

The first inequality in Eq. (91) is saturated by measuring the SSS along the direction where it is squeezed ( $y$ -axis, or equivalently measuring it in  $z$ -basis after applying a  $R_x(\frac{\pi}{2})$  pulse [35]). The second inequality originates from the uncertainty principle (Eq. (88)). Since the optimal SSS saturate the Heisenberg uncertainty relation [36] and the SSS generated by the adiabatic method [31] belongs to these states, we obtain the relation between the squeezing parameter and CFI

$$\text{CFI} = N/\xi^2. \quad (92)$$

Based on the data shown in Fig.3 from ref. (31), it takes about  $200\mu\text{s}$  for the adiabatic method to prepare an 8-spin SSS with  $\xi^2 = 0.4$  which corresponds to  $\text{CFI} = 20$ . The 2D spin density  $8/(30\text{nm} \times 30\text{nm})$  corresponds to  $\bar{f}_{dd} = 43.5\text{kHz}$ . According to Fig.3(d) in the main text, the variational method is able to prepare an 8-spin entangled state with  $\text{CFI} \approx 20$  by a 4-layer circuit with  $\bar{f}_{dd}T = 0.8$ . Plugging in the same average nearest neighbor dipolar interaction strength  $\bar{f}_{dd}$ , we finally calculated the state preparation time of the variational method is  $T = 18.4\mu\text{s}$ , which is about 11 times faster than the adiabatic method under the same condition.

#### Supplementary Note 9: Numerically solving Schrödinger and Lindblad equations

In this work, both the Schrodinger equations for unitary evolution and Lindblad master equations for noisy evolution are not solved via diagonalization, since the matrix dimension increases exponentially with the spin ensemble size and makes the computation ineffective and memory-consuming. In particular, for noisy cases, using the superoperator formalism would lead to a dimension growth of  $4^N$ . For 10 spins, the dimension would exceed one million. Instead, the equations are solved with linear multistep methods, which are well-suited numerical integrators to solve ordinary differential equations in the form of  $\frac{dy}{dt} = f(y, t)$ ,  $y(t_0) = y_0$ . Depending on the stiffness of the equation, implicit Adams method (for nonstiff) and backward differentiation formulas (for stiff) are applied. In simple words, the approximated values for  $y$  at previous time steps initialize slopes  $f$ , which are then interpolated by a polynomial. Replacing the original integrand by the interpolation polynomial gives a new approximated  $y$ , solved via an implicit equation. These methods are provided by `scipy.integrate.ode` of the `scipy` package of Python, setting the integrator to be “`zvode`”, meaning complex-valued variable-coefficient ODE solver. Details of the algorithm are described in [37].

#### SUPPLEMENTARY DISCUSSION: CONTROLLABILITY

Since all the black-box optimization algorithms cannot ensure that the optimized result is the global maximum/minimum point of in the parameter space, it is still an open question that if the variational method is able to find the ‘best’ metrological state for a given spin configuration or not. In this section, we’re interested in the theoretically achievable controllability of dipolar interacting spin systems. The question is, given any (possibly infinite) arbitrary sequence of evolution under each Hamiltonian governing the dynamics of our system, can we drive any arbitrary unitary operator? Quantum control systems of the general form

$$H(t) = H_0 + \sum_{k=1}^K u_k(t) H_k, \quad (93)$$

governed by the Schrödinger equation,  $i \frac{d}{dt} |\psi(t)\rangle = H(t) |\psi(t)\rangle$ , have been studied extensively [38,39,40].  $H_0$  is the unperturbed or free evolution Hamiltonian,  $H_k$  are the control interactions, and  $u_k(t)$  are the piecewise continuous control fields. There are several distinct but related notions of controllability that have different conditions for ‘full’ controllability. The notion of ‘operator’ or ‘complete’ controllability is the strictest condition and is defined as above. For generic interacting spin systems, all of these notions are equivalent. Complete controllability is equivalent to universal quantum computation (UQC) in quantum information processing (QIP) [41,42].

### Controllability Test

The way we investigate the controllability of a generic system (Eq. 93) is by examining the so-called ‘dynamical Lie algebra’  $\mathcal{L}_0 \subseteq u(\mathcal{N})$  or  $su(\mathcal{N})$  generated by the operators  $\{-iH_0, -iH_1, \dots, -iH_K\}$ , which are represented by  $\mathcal{N} \times \mathcal{N}$  matrices in a basis we choose [38,39].

A quantum system of the form (Eq. 93) is completely controllable if either  $\mathcal{L}_0 \cong u(\mathcal{N})$  or  $\mathcal{L}_0 \cong su(\mathcal{N})$  [38], where  $u(\mathcal{N})$  is the unitary Lie algebra represented by the set of skew-Hermitian  $\mathcal{N} \times \mathcal{N}$  matrices and  $su(\mathcal{N})$  is the special unitary Lie algebra represented by the same set of matrices with the extra condition that they are traceless. Note that  $\dim u(\mathcal{N}) = \mathcal{N}^2$  and  $\dim su(\mathcal{N}) = \mathcal{N}^2 - 1$ , and the difference of 1 comes from counting identity operation ( $I$ ) as a dimension or not. We must find a basis for  $\mathcal{L}_0$  by iteratively taking the Lie bracket  $[\cdot, \cdot]$  of  $H_0, H_1, \dots, H_K$  until we have a set of  $\dim \mathcal{L}_0$  linearly independent matrices, where the Lie bracket is the commutator  $[A, B] = AB - BA$  for matrices  $A$  and  $B$ . Ref.[38] and ref.[39] present an algorithm for generating this basis. Thus, if  $\dim \mathcal{L}_0 = \mathcal{N}^2$  or  $\mathcal{N}^2 - 1$  we can say that the system is completely controllable. Note that for generic spin systems  $\mathcal{N} = 2^N$  for  $N$  spins.

### Controllability of Dipolar Interacting Spin Systems

We write our system in the form (Eq. 93) by defining the free evolution Hamiltonian to be the dipolar interaction  $H_{dd}$  and two control interactions  $J_x$  and  $J_y$ , as these operators are generators of rotation, with respective independent control fields  $\theta_x(t)$  and  $\theta_y(t)$ :

$$H(t) = H_{dd} + \theta_x(t)J_x + \theta_y(t)J_y. \quad (94)$$

Ref.[39,43] demonstrate that we cannot achieve complete controllability with global controls due to inherent symmetries, so we know that  $\dim \mathcal{L}_0 < 4^N - 1$ .

However, complete controllability is a rather strict condition. Not being able to drive any arbitrary unitary does not mean we cannot drive unitaries that produce metrological states.

In fact, ref.[44] demonstrate for a long-range Ising spin model (all-to-all interactions) with global controls that metrological states, such as the GHZ and W states are reachable. Ref.[45] extend their result for symmetric Ising spin networks with global controls and demonstrate that one can reach any state that preserves spin permutation invariance. This is known as subspace controllability. The dimension of their dynamical Lie algebra,  $\mathcal{L}^{\text{Ising}} \equiv \mathcal{L}^{\text{PI}} \cap su(2^N)$ , is

---

#### Algorithm. Generating $\mathcal{L}_0$ and finding $\dim \mathcal{L}_0$ .

---

*Input:* Hamiltonians  $I \equiv \{H_0, H_1, \dots, H_K\}$

1.  $B \equiv$  maximal linearly independent subset of  $I$
  2.  $r \equiv |B|$
  3. If  $r = N^2$  then  $O \equiv B$  else  $O \equiv \{\}$
  4. If  $r = N^2$  or  $|B| = 0$  then terminate
  5.  $C \equiv [O, B] \cup [B, B]$ , where  
 $[S_1, S_2] \equiv \{[s_1, s_2] \mid s_1 \in S_1, s_2 \in S_2\}$
  6.  $O = O \cup B$
  7.  $B =$  maximal linearly independent extension of  $O$  with  
elements from  $C$
  8.  $r = r + |B|$ ; Go to 4
- Output:* basis  $O$  of  $\mathcal{L}_0$  and  $\dim \mathcal{L}_0 = r$
- 

**Supplementary Table 2.** Implementation of [39]’s algorithm with a few physically motivated modifications. Note  $|S|$  indicates the cardinality of set  $S$ .

Lie algebra dimension	$N = 2$	$N = 3$	$N = 4$	$N = 5$
Completely controllable: $4^N$ (or $4^N - 1$ )	16	64	256	1024
$H_{dd}$	9	39	225	
Symmetric Ising: $\binom{N+3}{N} - 1$	9	19	34	55

**Supplementary Table 3.** Lie algebra dimensions for the complete controllable system, dipolar interacting system and symmetric Ising system (lower bound for subspace controllability). Dipolar interacting spin systems'  $\dim \mathcal{L}_0$  is calculated using an implementation of [39]'s algorithm, and is necessarily bounded by the complete and subspace controllability dimensions. Lie algebra dimensions for dipolar interacting systems are only calculated up to  $N = 4$  due to stability issues stemming from numerical errors in how matrix rank is calculated.

shown to be  $\binom{N+3}{N} - 1$ . This is relevant to our system because [46] show that if we replace the Ising interaction with a more general two body interaction—which includes  $H_{dd}$ —the dimension of the dynamical Lie algebra is necessarily greater than or equal to that of the symmetric Ising case, and it is therefore subspace controllable. This means that we can write  $\binom{N+3}{N} - 1 \leq \dim \mathcal{L}_0 < 4^N - 1$  and say that  $\mathcal{L}_0$  is subspace controllable but not completely controllable. Therefore, we can achieve arbitrary permutation invariant states, including metrological states such as a GHZ state.

### Finding Reachable States

$\mathcal{L}_0$  is associated with a Lie group  $e^{\mathcal{L}_0}$  by the Lie group–Lie algebra correspondence [38]. The Lie algebra  $u(\mathcal{N})$  corresponds to the Lie group  $U(\mathcal{N})$ , and  $su(\mathcal{N})$  corresponds to  $SU(\mathcal{N})$ . We can define  $\mathcal{R} \equiv e^{\mathcal{L}_0}$  as the reachable set of unitaries we can drive under  $\{H_k\}_{k=0,\dots,K}$ , and so starting from an initial state  $|\psi_0\rangle$ ,  $\mathcal{R}_{|\psi_0\rangle}$  is the set of states we can reach.

As demonstrated in the previous section, our dynamical Lie algebra is a superset of  $\mathcal{L}^{\text{Ising}}$  and a strict subset of  $su(2^N)$ , so we can write  $e^{\mathcal{L}^{\text{Ising}}} \subseteq e^{\mathcal{L}_0} \subset SU(2^N)$ . Because  $|\text{GHZ}\rangle \in \mathcal{R}_{|0\rangle^{\otimes N}}^{\text{Ising}}$  we can write  $|\text{GHZ}\rangle \in \mathcal{R}_{|0\rangle^{\otimes N}}^{\text{dipolar}}$ . In fact, this is true for any permutation invariant state, which includes all metrological states we're interested in.

While we know that metrological states are in the reachable set, determining the parameters that drive the unitaries to produce those states is a highly convex optimization problem equivalent to our variational circuit, using state fidelity between the ideal state and the current state instead of CFI as the cost function. That is we optimize the output unitary of the variational circuit,

$$\mathcal{S}(\boldsymbol{\theta}) = e^{-i\frac{\pi}{2}J_y} \prod_{i=1}^m e^{-i\tau_i H_{dd}} e^{-i\vartheta_i J_x} e^{i\frac{\pi}{2}J_y} e^{-i\tau'_i H_{dd}} e^{-i\frac{\pi}{2}J_y}, \quad (95)$$

where  $m$  is the (possibly infinite) number of layers, for state fidelity,

$$\mathcal{F}(|\text{GHZ}\rangle, \mathcal{S}(\boldsymbol{\theta}) |0\rangle^{\otimes N}) = \left| \langle \text{GHZ} | \mathcal{S}(\boldsymbol{\theta}) |0\rangle^{\otimes N} \right|^2, \quad (96)$$

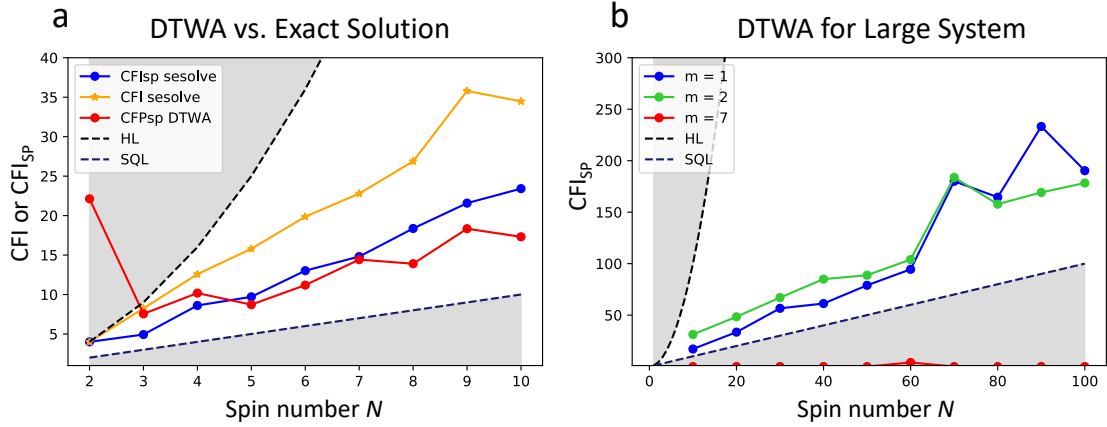
for pure states. If there exists some  $\boldsymbol{\theta}$  such that  $\mathcal{F}(|\text{GHZ}\rangle, \mathcal{S}(\boldsymbol{\theta}) |0\rangle^{\otimes N}) = 1$ , then we can say that  $|\text{GHZ}\rangle \in \mathcal{R}_{|0\rangle^{\otimes N}}^{\text{dipolar}}$ . From the previous section, we know such a  $\boldsymbol{\theta}$  must exist, but it may be the case that  $m \rightarrow \infty$ , in which case it is not possible to find this exactly. This is the method employed in ref.[44,47] to demonstrate the reachability of GHZ and W states for Ising spin models. Our variational circuit method represents an improvement in the efficiency of searching for such metrological states.

## SUPPLEMENTARY METHODS

### Large spin number ( $N \rightarrow 100$ ) optimization: discrete truncated Wigner approximation (DTWA)

The optimization results for small spin number ( $N \leq 10$ ) are of particular interest to nanoscale quantum sensing, where the sensor size limits  $N$ . On the other hand, the advantage of Heisenberg limit quantum sensing ( $\frac{1}{N}$ ) becomes more dominant compared to stand quantum limit sensing ( $\frac{1}{\sqrt{N}}$ ) when the spin number  $N$  is large. Thus, it is worth to discuss the performance of the variational method in large  $N$  case. However, numerically simulate large  $N$  system is challenging because the Hilbert space grows exponentially.

We employ discrete truncated Wigner approximation (DTWA) [48,49], Monte Carlo algorithm, to semi-classically simulate the time evolution of large interacting spin system. Instead of using a  $2^N$  dimensional density matrix (or state vector) to describe the spin system, DTWA represent each spin by a 3-dimensional vector  $(s_i^x, s_i^y, s_i^z)$ , where  $s_i^{x,y,z}$  are real numbers that stand for the spin components for number  $i$ 'th spin. The initial values of  $s_i^{x,y,z}$  are randomly sampled following the probability distribution of the initial quantum state and the time evolution of  $s_i^{x,y,z}$  is described by a classical Hamiltonian equation [48]. The final time evolution results are obtained by averaging the results from different initial values of  $s_i^{x,y,z}$ .



**Supplementary Figure 11. DTWA optimization results:** In 2D square lattice spin configuration. (a) Sanity check for  $N = 2 - 10$ , circuit layer  $m = 1$ . Results from the optimizer using the exact Schrödinger equation solver (sesolve) and DTWA are shown. (b) Optimization up to  $N = 100$  by using DTWA, circuit layer  $m = 1, 2, 7$ .

Due to the statistical nature of the Monte Carlo simulation, DTWA is not compatible with parameter shift, the way we previously computed the cost function [19,20,21]. Thus, we use the  $\text{CFI}_{\text{SP}}$  of a Gaussian states which related to the squeezing parameter as the cost function for DTWA optimization (derived in Eq. 92). Figure 11(a) shows the optimized data by using DTWA and exact numerical simulation (sesolve function in QuTip) for the 2D square lattice spin configuration when  $N \leq 10$ . We observed that the optimized results from DTWA are lower than those from the exact simulation when  $N > 5$ . This can be attributed to the statistical fluctuation induced by the DTWA algorithm and its influence to the landscape of the parameter space which might be harder to optimize. Note, the unphysical beyond-HL sensitivity for  $N = 2$  is an example where DTWA fails in describing a highly entangled state. Based on the  $\text{CFI} = \text{CFI}_{\text{SP}} = 4$  result by using the exact numerical simulation, we know that a GHZ state (Bell pair) is generated and DTWA is not able to correctly capture the properties of such highly entangled state.

In Fig. 11(b), the optimized  $\text{CFI}_{\text{SP}}$  of 1, 2 and 7 layer circuit for spin number up to 100 are shown. Beyond-SQL sensitivity is still reached in 1 and 2 layer circuits' results. Note, the circuits for  $m=1$  (and  $m=2$ ) are a sub-set of  $m=7$ , yet the shallower circuits outperform  $m=7$  in DTWA. We attribute this to CMA-ES failing to optimize the cost function in a large dimensional space, which is particularly difficult given the statistical nature of DTWA.

The DTWA optimization results indicate that our approach is promising to realize beyond-SQL quantum sensing for 2D spin systems, even when the spin number is large and the circuit shallow. However, further investigations regarding scalability of our variational method on 2D random/3D random spin configurations is needed. More robust optimization algorithms that are compatible with large  $N$  and  $m$  would likely further the improvements. On the other hand, running the optimization directly on the experimental platform will potentially get around the difficulty of simulating large spin ensembles precisely and optimize for suitable quantum states under all kinds of experimental imperfections.

## SUPPLEMENTARY REFERENCES

---

- [1] B. Koczor, R. Zeier, and S. J. Glaser, Fast computation of spherical phase-space functions of quantum many-body states, *Phys. Rev. A* **102**, 062421 (2020).
- [2] G. Kucsko *et al.*, Critical thermalization of a disordered dipolar spin system in diamond, *Phys. Rev. Lett.s* **121**, 023601 (2018).
- [3] C. Slichter, Principles of magnet resonance, Spring Series in Solid (1980).
- [4] S. Choi *et al.*, Observation of discrete time-crystalline order in a disordered dipolar many-body system, *Nature* **543**, 221–225 (2017).
- [5] A. Rényi, On measures of entropy and information, in *Proceedings of the Fourth Berkeley Symposium on Mathematical Statistics and Probability, Volume 1: Contributions to the Theory of Statistics*, Vol. 4 (University of California Press, 1961) p. 547–562.
- [6] R. Horodecki, P. Horodecki, M. Horodecki, and K. Horodecki, Quantum entanglement, *Rev. Mod. Phys.* **81**, 865 (2009).
- [7] R. o. Islam, Measuring entanglement entropy in a quantum many-body system, *Nature* **528**, 77–83 (2015).
- [8] M. M. Wolf, F. Verstraete, M. B. Hastings, and J. I. Cirac, Area laws in quantum systems: mutual information and correlations, *Phys. Rev. Lett.s* **100**, 070502 (2008).
- [9] D. Bluvstein *et al.*, A quantum processor based on coherent transport of entangled atom arrays, *Nature* **604**, 451–456 (2022).
- [10] R. S. Sutton and A. G. Barto, *Reinforcement learning: An introduction* (MIT press, 2018).
- [11] D. Silver *et al.*, Mastering the game of Go without human knowledge, *Nature* **550**, 354–359 (2017).
- [12] P. Peng, X. Huang, C. Yin, L. Joseph, C. Ramanathan, and P. Cappellaro, Deep reinforcement learning for quantum Hamiltonian engineering, Preprint at <https://arxiv.org/abs/2102.13161> (2021).
- [13] M. A. Nielsen and I. L. Chuang, *Quantum Computation and Quantum Information* (Cambridge University Press, 2010).
- [14] R. Kaubruegger *et al.*, Variational spin-squeezing algorithms on programmable quantum sensors, *Phys. Rev. Lett.s* **123**, 260505 (2019).
- [15] R. Kaubruegger, D. V. Vasilyev, M. Schulte, K. Hammerer, and P. Zoller, Quantum variational optimization of Ramsey interferometry and atomic clocks, *Phys. Rev. X* **11**, 2160 (2021).
- [16] B. Yan *et al.*, Observation of dipolar spin-exchange interactions with lattice-confined polar molecules, *Nature* **501**, 521–525 (2013).
- [17] S. L. Braunstein and C. M. Caves, Statistical distance and the geometry of quantum states, *Phys. Rev. Lett.s* **72**, 3439 (1994).
- [18] H. Strobel *et al.*, Fisher information and entanglement of non-gaussian spin states, *Science* **345**, 424–427 (2014).
- [19] M. Cerezo *et al.*, Variational quantum algorithms, *Nat. Rev. Phys.* , 1–20 (2021).
- [20] J. J. Meyer, J. Borregaard, and J. Eisert, A variational toolbox for quantum multi-parameter estimation, *NPJ Quantum Inf.* **7**, 1–5 (2021).
- [21] M. Schuld, V. Bergholm, C. Gogolin, J. Izaac, and N. Killoran, Evaluating analytic gradients on quantum hardware, *Phys. Rev. A* **99**, 032331 (2019).
- [22] R. Krischek, C. Schwemmer, W. Wieczorek, H. Weinfurter, P. Hyllus, L. Pezzé, and A. Smerzi, Useful multiparticle entanglement and sub-shot-noise sensitivity in experimental phase estimation, *Phys. Rev. Lett.* **107**, 080504 (2011).
- [23] D. Panchenko, Properties of MLE: consistency, asymptotic normality. Fisher information, (unpublished).
- [24] A. Smirne, J. Kołodyński, S. F. Huelga, and R. Demkowicz-Dobrzański, Ultimate precision limits for noisy frequency estimation, *Phys. Rev. Lett.s* **116**, 120801 (2016).
- [25] I. Bengtsson and K. Zyczkowski, *Geometry of Quantum States* (Cambridge University Pres, 2006).
- [26] H.-P. Breuer and F. Petruccione, *The Theory of Open Quantum Systems* (Oxford University Pres, 2002).
- [27] E. Andersson, J. D. Cresser, and M. J. W. Hall, Finding the kraus decomposition from a master equation and vice versa, *J. Mod. Opt.* **54**, 1695 (2007).
- [28] A. S. Holevo, A note on covariant dynamical semigroups, *Rep. Math. Phys.* **32**, 211–216 (1993).
- [29] J. R. Johansson, P. D. Nation, and F. Nori, Qutip: An open-source python framework for the dynamics of open quantum systems, *Comput. Phys. Commun.* **183**, 1760 (2012).
- [30] L. Jiang *et al.*, Repetitive readout of a single electronic spin via quantum logic with nuclear spin ancillae, *Science* **326**, 267–272 (2009).
- [31] P. Cappellaro and M. D. Lukin, Quantum correlation in disordered spin systems: Applications to magnetic sensing, *Phys. Rev. A* **80**, 032311 (2009).
- [32] D. J. Wineland, J. J. Bollinger, W. M. Itano, and D. Heinzen, Squeezed atomic states and projection noise in spectroscopy, *Phys. Rev. A* **50**, 67 (1994).
- [33] L. Pezzé and A. Smerzi, Entanglement, Nonlinear Dynamics, and the Heisenberg Limit, *Phys. Rev. Lett.s* **102**, 100401 (2009).
- [34] P. Hyllus, O. Gühne, and A. Smerzi, Not all pure entangled states are useful for sub-shot-noise interferometry, *Phys. Rev. A* **82**, 012337 (2010).

- [35] E. Pedrozo-Peñafield *et al.*, Entanglement on an optical atomic-clock transition, *Nature* **588**, 414–418 (2020).
- [36] L. Pezze, A. Smerzi, M. K. Oberthaler, R. Schmied, and P. Treutlein, Quantum metrology with nonclassical states of atomic ensembles, *Rev. Mod. Phys.* **90**, 035005 (2018).
- [37] G. D. Byrne and A. C. Hindmarsh, A polyalgorithm for the numerical solution of ordinary differential equations, *ACM Trans. Math. Softw.* **1**, 71–96 (1975).
- [38] D. d’Alessandro, *Introduction to quantum control and dynamics* (Chapman and hall/CRC, 2021).
- [39] S. G. Schirmer, H. Fu, and A. I. Solomon, Complete controllability of quantum systems, *Phys. Rev. A* **63**, 063410 (2001).
- [40] N. Khaneja, R. Brockett, and S. J. Glaser, Time optimal control in spin systems, *Phys. Rev. A* **63**, 032308 (2001).
- [41] X. Wang, D. Burgarth, and S. Schirmer, Subspace controllability of spin-1/2 chains with symmetries, *Phys. Rev. A* **94**, 052319 (2016).
- [42] V. Ramakrishna and H. Rabitz, Relation between quantum computing and quantum controllability, *Phys. Rev. A* **54**, 1715 (1996).
- [43] T. Polack, H. Suchowski, and D. J. Tannor, Uncontrollable quantum systems: A classification scheme based on Lie subalgebras, *Phys. Rev. A* **79**, 053403 (2009).
- [44] J. Chen, H. Zhou, C. Duan, and X. Peng, Preparing Greenberger-Horne-Zeilinger and W states on a long-range Ising spin model by global controls, *Phys. Rev. A* **95**, 032340 (2017).
- [45] F. Albertini and D. D’Alessandro, Controllability of symmetric spin networks, *J. Math. Phys.* **59**, 052102 (2018).
- [46] F. Albertini and D. D’Alessandro, Subspace controllability of multi-partite spin networks, *Syst. Control. Lett.* **151**, 104913 (2021).
- [47] Y. Gao, H. Zhou, D. Zou, X. Peng, and J. Du, Preparation of Greenberger-Horne-Zeilinger and w states on a one-dimensional Ising chain by global control, *Phys. Rev. A* **87**, 032335 (2013).
- [48] J. Schachenmayer, A. Pikovski, and A. M. Rey, Many-body quantum spin dynamics with monte carlo trajectories on a discrete phase space, *Phys. Rev. X* **5**, 011022 (2015).
- [49] M. A. Perlin, C. Qu, and A. M. Rey, Spin squeezing with short-range spin-exchange interactions, *Phys. Rev. Lett.s* **125**, 223401 (2020).